Ph.D. Dissertation of Medicine

Analysis of new location-adaptive threshold method in coronary artery segmentation and blooming artifact from calcification using computed tomography

전산화 단층촬영 영상을 이용한 관상동맥 분할의 새로운 위치 적응형 한계치 방법 및 칼슘의 블루밍 아티팩트 분석 연구

February 2023

Graduate School of Medicine
Seoul National University
Clinical Medical Sciences Major

Daebeom Park

Analysis of new location-adaptive threshold method in coronary artery segmentation and blooming artifact from calcification using computed tomography

Examiner: Whal Lee

Submitting a Ph.D. Dissertation of
Medicine
October 2022

Graduate School of Medicine
Seoul National University
Clinical Medical Sciences Major

Daebeom Park

Confirming the Ph.D. Dissertation written by
Daebeom Park
January 2023

Chair	_____	(Seal)
Vice Chair	_____	(Seal)
Examiner	_____	(Seal)
Examiner	_____	(Seal)
Examiner	_____	(Seal)

Abstract

Analysis of new location-adaptive threshold method in coronary artery segmentation and blooming artifact from calcification using computed tomography

Daebeom Park

Department of Clinical Medical Sciences

The Graduate School

Seoul National University

Part 1. Analysis of new location-adaptive threshold method in coronary artery segmentation using computed tomography

Introduction

An automatic segmentation technique of coronary artery using coronary computed tomography angiography images can provide several analyses related to the coronary artery disease (CAD) and

the accurate segmentation of lumen or plaque region is one of the most important factors. This research aimed to analyze the performance of the segmentation algorithm of a newly developed software platform with new location-adaptive threshold method (NLATM) by comparing the result with the commercially available software platforms.

Materials and Methods

Data sets from intravascular ultrasound (IVUS) for 26 vessel segments of 19 patients were used as gold standards. Performance of the segmentation algorithm of several software platforms was analyzed by using the data of lumen or plaque parameters of the target segments. Statistical analyses (Pearson correlation coefficient [PCC], intraclass correlation coefficient [ICC], and Bland-Altman plot) were conducted for lumen or plaque parameters by comparing the data sets of each software platform with IVUS.

Results

Software platform with NLATM showed the bias closest to zero for detecting lumen volume (mean difference = −9.1 mm^3, 95% confidence interval [CI] = −18.6 to 0.4 mm^3) or area (mean

difference = −0.72 mm^2, 95% CI = −0.80 to −0.64 mm^2) with the highest PCC and ICC. Moreover, subgroup lumen or plaque area analyses were conducted and software platform with NLATM showed the bias closest to zero for detecting lumen (mean difference = −0.07 mm^2, 95% CI = −0.16 to 0.02 mm^2) or plaque area (mean difference = 1.70 mm^2, 95% CI = 1.37 to 2.03 mm^2) in the stenotic region with significantly higher correlation coefficient than other commercially available software platforms ($p < 0.001$).

Conclusion

Consequently, the result shows that the newly developed software platform with NLATM has potential for serving as an aiding system for evaluation of CAD.

Part 2. Analysis of blooming artifact from calcification using computed tomography

Introduction

Computed tomography (CT) is a well-known non-invasive modality used for the diagnosis of CAD. However, blooming artifact from calcification appearing in CT images leads to underestimation

of the actual coronary artery lumen size. Several studies suggested the CT scan using higher X-ray energy levels for reducing blooming artifact from calcification with subjective visual assessment. This phantom study aimed to evaluate the effect of higher X-ray energy levels with objective quantitative measurement of adjacent affected pixel from calcification using CT images

Materials and Methods

A phantom was manufactured considering various shapes and sizes of calcium. CT images were acquired from three different dual energy CT scanners (Siemens [vendor 1], Philips [vendor 2], and GE [vendor 3]) by changing the setting of X-ray energy parameters such as kilovoltage peak (kVp) and kilo-electron volts (keV) levels using the manufactured phantom. Adjacent affected pixel from calcification was analyzed by measuring the brightened region excluding the actual calcified region determined by full width at third maximum which calculated the calcified region with error close to zero (mean error = 0.05 mm and standard error of mean = 0.01 mm).

Results

The result showed that the change in kVp levels failed to reduce adjacent affected pixel from calcification in reconstructed polychromatic CT images (Field of view [FOV] 300 mm, p = 0.167, 0.494, and 0.861; FOV 150 mm, p = 0.150, 0.161, and 0.075 for vendor 1, 2, and 3). Moreover, change in keV levels showed different aspects of adjacent affected pixel from calcification in reconstructed virtual monochromatic images with three dual energy implementation methods (FOV 300 mm, no significant difference [p = 0.191], increase [p < 0.001], and decrease [p <0.001] for vendor 1, 2, and 3).

Conclusion

Objective quantitative measurement shows no relationship between higher X-ray energy levels and adjacent affected pixel from calcification.

Keyword: coronary artery disease, computed tomography, new location-adaptive threshold method, blooming artifact, X-ray energy, adjacent affected pixel from calcification

Student Number: 2021-39269

Table of Contents

List of Figures

List of Tables

Part 1. Analysis of new location-adaptive threshold method in coronary artery segmentation using computed tomography

Chapter 1. Introduction

Coronary artery disease (CAD) is the leading cause of mortality worldwide, which can induce various diseases related to cardiovascular system and the number of CAD patients is rapidly increasing in the world (1-4). To evaluate CAD, coronary computed tomography angiography (CCTA) is used, which has been a critical tool for diagnosing CAD (5-8). Using CCTA images, an automatic segmentation technique of coronary arteries can be performed and several analyses related to the CAD are possible (9, 10). Moreover, detection of the degree of coronary stenosis using the segmented three-dimensional (3D) model might be helpful when an expert evaluation is not available (11). Currently, several methods are available for coronary segmentation, however, they require manual segmentation processes to generate an accurate 3D model of coronary arteries which induce intra- and inter- observer variability (12-14).

Stenosis severity of lumen is an important factor for diagnosing

CAD because the blood flow decreases in the stenotic region of vessels (15, 16). In addition, the components of plaque, including lipids and calcium in blood vessels, are also very important factors in diagnosing CAD (17, 18). The evaluation of CAD can be determined by the amount of lipid in the vessel of coronary artery, and ischemic heart failure can be induced if the lipid-rich plaques rupture in the vessel (18, 19). Using CCTA images, an automatic segmentation technique of coronary arteries can be performed and the calculation of lumen or plaque volume is possible (9, 10). Accurate detection of lumen or plaque volume in the stenotic region using an automatic segmentation technique is required for providing several useful analytic tools in diagnosing CAD. However, there are only a few studies that validated segmentation techniques for plaque volume because detecting the outer wall is generally more challenging than lumen (20).

Previous study showed that the location-adaptive threshold method (LATM) could overcome the segmentation of coronary arteries in the region of stenosis (21). A new location-adaptive threshold method (NLATM) was developed and a software platform with NLATM (software 1) was released. The performance of the lumen or plaque segmentation algorithm of software 1 was analyzed

by comparing the result with the commercially available software platforms (software 2 and 3). Data sets of coronary lumen or plaque parameters (area and volume) from intravascular ultrasound (IVUS) for 26 vessel segments of 19 patients were used as gold standards. The performance of the segmentation algorithm of several software platforms was analyzed by using the data set of lumen or plaque parameters at a fixed interval for a specific length of the target vessel segments. Statistical analyses (Pearson correlation coefficient [PCC], intraclass correlation coefficient [ICC], and Bland–Altman plot) were conducted for lumen or plaque parameters by comparing the data sets of each software platform with IVUS.

Software 1 showed the best performance for detecting lumen volume or area. PCC and ICC were the highest with the bias closest to zero for lumen volume (PCC = 0.92, 95% confidence interval [CI] = 0.83 to 0.97; ICC = 0.91, 95% CI = 0.79 to 0.96; mean difference = −9.1 mm^3, 95% CI = −18.6 to 0.4 mm^3) or area (PCC = 0.79, 95% CI = 0.77 to 0.80; ICC = 0.76, 95% CI = 0.66 to 0.82; mean difference = −0.72 mm^2, 95% CI = −0.80 to −0.64 mm^2) when compared software 1 with IVUS. Moreover, subgroup lumen or plaque area analyses were conducted and software 1 showed the

best performance for detecting lumen or plaque area in the stenotic region. PCC and ICC were the highest with the bias closest to zero for lumen (PCC = 0.62, 95% CI = 0.57 to 0.66; ICC = 0.61, 95% CI = 0.56 to 0.65; mean difference = −0.07 mm^2, 95% CI = −0.16 to 0.02 mm^2) or plaque area (PCC = 0.52, 95% CI = 0.47 to 0.58; ICC = 0.36, 95% CI = 0.25 to 0.44; mean difference = 1.70 mm^2, 95% CI = 1.37 to 2.03 mm^2) in the stenotic region when compared software 1 with IVUS. Software 1 showed significantly outstanding performance in detecting lumen or plaque area in stenotic region than commercially available software platforms ($p < 0.001$). Consequently, the result shows that the newly developed software platform with NLATM have a potential for serving as an aiding system for evaluation of CAD.

Chapter 2. Materials and Methods

This work was funded by AI Medic Inc. The CCTA images included in this study were absent during the development of the software platform with NLATM. Institutional Review Board reviewed and approved the retrospective nature of this study and waived the requirement to obtain informed consent (IRB No. 2107-192-1237). Methods for 1) subjects, 2) CCTA image acquisition and reconstruction, and 3) IVUS imaging protocol and analysis were adopted from the previous research (21).

2.1. Subjects

30 target coronary segments of 22 patients were included in this study. The patients with suspected or known CAD went through CCTA and clinically indicated invasive coronary angiography with IVUS at Seoul National University Hospital from March 1, 2009 to June 30, 2010. The exclusion criterion was made with the poor CCTA image quality in the target segment due to motion artifacts (n = 4). Overall, 26 target coronary segments of 19 patients were included in this study (average age, 64.6 years; female, 15.3%). 19 and remaining 7 target segments contained partially calcified

plaques and only non-calcified plaques, respectively. Failure criteria of segmentation for each software were made with following conditions: i) failure to open files in the format of Digital Imaging and Communications in Medicine (DICOM); (ii) difference of more than 100 mm^3 (lumen volume); (iii) 200 mm^3 (plaque volume); (iv) 7 mm^2 (lumen area); (v) 13 mm^2 (plaque area) between the results measured by a dedicated software platform and IVUS. Failure rate of each condition for different software platforms is shown in Supplementary Table S1.

2.2. CCTA Image Acquisition and Reconstruction

In accordance with guidelines for the Society of Cardiovascular Computed Tomography, CCTA images were acquired (22). CCTA was conducted with a dual- source, a 16-slice, or a 256-slice CT scanner (SOMATOM Definition Siemens Healthineers; Sensation 16, Siemens Healthineers; iCT, Philips Healthcare) (n = 17, 8, and 1). The scan parameters were set as follows: (a) collimation = 32 x 0.6 mm / 16 x 0.75 mm / 128 x 0.625 mm; (b) a tube voltage = 100 kVp or 120 kVp; (c) tube currents = 104-620 mA; (d) rotation times = 270-370 ms. A tube voltage and currents were set

depending on body habitus. A mono-segment reconstruction algorithm was used for generating the images with a retrospective electrocardiographic-gated technique. Reconstruction parameter were set as follows: (a) slice thickness = 0.8-1 mm; (b) increments = 0.5-0.7 mm; (c) kernel = a medium soft convolution kernel. CCTA data were collected with motion-free and typically in the mid-diastolic phase.

2.3. IVUS Imaging Protocol and Analysis

To acquire the images using IVUS, a 40 MHz, 2.9 F catheter (Boston Scientific Scimed) was used with an axial and lateral resolution of ± 80 and ± 200 μm, respectively. IVUS imaging was performed all through the length of target segments after given intracoronary nitroglycerine. A pullback system with a standard automated motor was used for acquiring IVUS images by measuring cross-sectional area at a speed of 0.5 mm/s with 30 frames/s. A computerized software (echoPlaque, INDEC Medical Systems, Inc.) was used for analyzing the target segments of the IVUS images by a cardiologist. To measure the lumen area, manual trace of lumen-intima interface and external elastic membrane was performed for

each cross-sectional plane. The Simpson's rule was employed for calculating volume parameters of each lesion using the cross-sectional areas. Side branches were used for the initial landmark for recording the location of target segments. On the 3D volume rendered images of CCTA, the location information was provided as references of the target segment including the documentation of the up or downstream direction with lesion lengths.

2.4. Measurement of Lumen or Plaque Parameters for Three Software Platforms

In this study, CCTA images and IVUS image data of 26 target coronary segments of 19 patients were used. The information of target segments was provided in IVUS data and 3D images with annotation were included. In addition, the data obtained from IVUS were organized in a Microsoft Excel sheet including the components such as the areas of lumen and plaque as well as plaque burden for each cross-sectional plane of a specific length of the target coronary segment. The performance of the dedicated software platforms (software 1 = AutoSeg, AiMedic; software 2 = Syngo.via, Siemens; software 3 = IntelliSpace Portal, Philips) was compared

using the data of IVUS as gold standards. For each software platform, the target vessel was found according to the provided image, and the lumen or plaque area was measured for each cross-sectional plane by a specific interval (Figure 2.1).

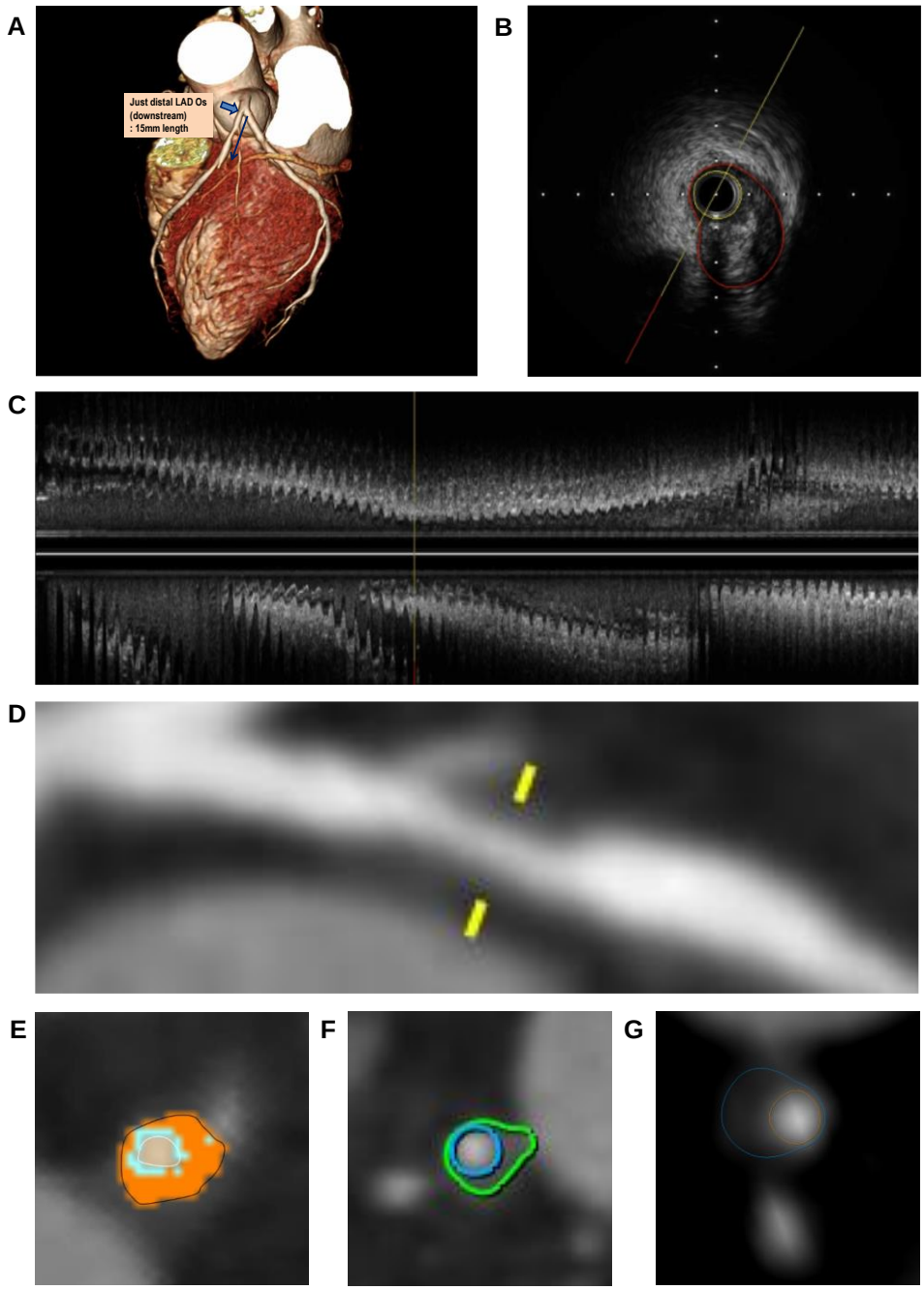

Figure 2.1. Representative images of the curved planar reformation and cross-sectional planes of lumen or plaque region for each software platform. (A) A location information annotated on a three-dimensional image of the coronary computed tomography

angiography that provided the reference to the exact length of the target segment. (B) The representative cross-sectional plane of IVUS. (C-D) Longitudinal and curved planar reformation images of the target segment of IVUS (C) and software (D), respectively. (E-G) The representative cross-sectional planes of software 1 (E), 2 (F), and 3 (G). Inner and outer lines (white and black for software 1; blue and green for software 2; orange and blue for software 3) represent lumen and vessel boundaries, respectively. Software 1 = AutoSeg, AiMedic; Software 2 = Syngo.via, Siemens; Software 3 = IntelliSpace Portal, Philips

The area graphs for one example case using each software platform are shown in Figure 2.2.

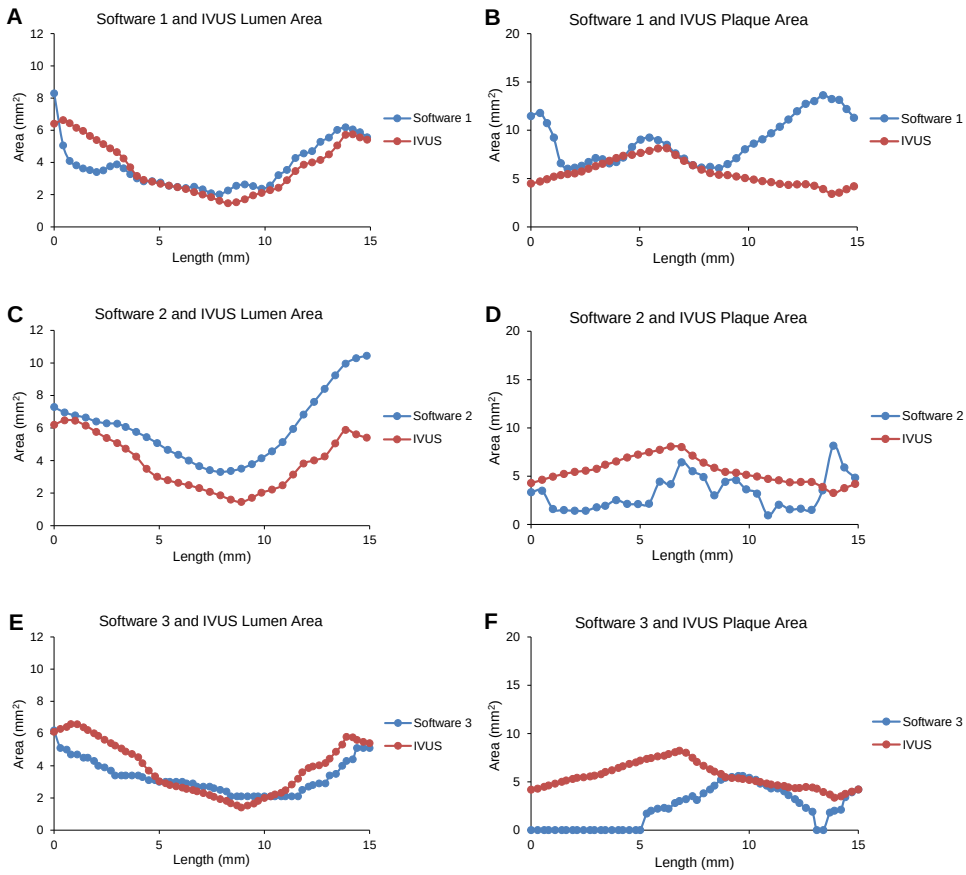

Figure 2.2. Representative graph plots of lumen or plaque area measured by each software platform against IVUS. Graph plots of lumen (A, C, and E) or plaque area (B, D, and F) measured by software 1 (A and B), 2 (C and D), or 3 (E and F) against IVUS. Software 1 = AutoSeg, AiMedic; Software 2 = Syngo.via, Siemens; Software 3 = IntelliSpace Portal, Philips

The interval of cross-sectional planes was different in IVUS data sets (0.001 mm) and software platforms (0.2-0.5 mm). Therefore,

the interval of IVUS data was adaptively modified to each software platform for comparing lumen or plaque area in each cross-sectional plane. The sum of lumen or plaque areas multiplied by the specific interval of each software platform was calculated for lumen or plaque volume. The calculated volume was compared with the provided volume of IVUS for each target coronary segment.

2.5. New Location-Adaptive Threshold Method for Calculating Lumen or Plaque Area

Lumen or plaque area measurement using NLATM was performed with a dedicated version of software platform (AutoSeg-H ver. 1.05; AI Medic Inc., Seoul, South Korea).

Software platform imports the files in the format of DICOM and uses artificial intelligence (AI) technology to extract the shape of the coronary artery (Supplementary Figure S1A). With the 3D model obtained through the AI technique using V-net (23), the skeleton of the coronary artery is generated considering the removal of calcified plaques and veins (Supplementary Figure S1B). Following the cross-sectional planes of the centerline extracted from the skeleton of the coronary vessel, a precise algorithm that

calculates and divides the coronary lumen and vessel boundaries is used by giving a NLATM instead of a fixed Hounsfield Unit (HU) (Supplementary Figure S1C–D). The calcium is excluded in lumen and included in vessel boundaries, therefore, detecting the calcium regions is important for calculating the exact boundary. For detecting calcium regions, software platform calculates a reference value for each CCTA datum through automatic segmentation of ascending aorta using a deep learning model (Supplementary Figure S1E). The model for segmenting the ascending aorta was trained with the neural network, Deeplab v3+ using the images treated with Gaussian mixture model–based expectation–maximization algorithm, histogram optimization algorithm, and Hessian filter (24–27). Using the attenuation values of segmented ascending aorta, the reference value is calculated with AI technique called Xgboost (28). The lumen and calcium regions are separated using the threshold in combination of the reference value from the segmented ascending aorta with the attenuation values of inner points in each cross–sectional plane of the centerline. After that, the surface of the coronary artery is smoothed through various post–processing algorithms and the final output is generated (Supplementary Figure S1F).

2.6. Subgroup Lumen or Plaque Area Analysis According to Plaque Burden

The given values of plaque burden from IVUS data were used for subgroup analysis of lumen or plaque areas. Plaque burden is the ratio of the plaque area to the vessel area. The total cross-sectional planes of coronary segments were divided into two groups of plaque burden > 0.6 and <= 0.6 (about 40% of total segments with plaque burden > 0.6). For subgroups with the stenotic (plaque burden > 0.6) and non-stenotic (plaque burden <= 0.6) regions, lumen or plaque area measured by three software platforms was compared to those derived by IVUS (Supplementary Table S2).

2.7. Statistical Analysis

For agreement analysis, the Bland-Altman plot was performed by illustrating the bias against the difference of the measurements (29). Definition of the limits of agreement was the mean difference minus and plus 1.96 times the standard deviation [SD] of the differences for the lower and upper limits, respectively. In addition

to Bland-Altman plot, PCC and ICC were used to evaluate the reliability of each software against the IVUS data (30, 31). ICC was applied using the two-way random effects, single measurement, and absolute agreement. For comparing correlation coefficient, Fisher's r-to-Z transformation was used based on independent groups (32). A p-value of 0.05 or less demonstrated a significant difference statistically. All analyses were performed using software, R version 4.2.0 package.

Chapter 3. Results

3.1. Comparison of Lumen or Plaque Volume for Three Different Software Platforms

To analyze the accuracy of lumen or plaque segmentation using different software platforms, the calculated lumen or plaque volume for each target segment was compared with IVUS. The statistical analysis of PCC and ICC of lumen or plaque volume for each software platform using IVUS data sets as gold standards is shown in Table 3.1 and Supplementary Figure S2.

Table 3.1. Pearson correlation coefficient and intraclass correlation coefficient of lumen or plaque volume of each software platform based on IVUS data sets.

		Software 1	Software 2	Software 3
Lumen volume	*r*†	0.92	0.91	0.92
	95% CI	0.83–0.97	0.78–0.96	0.83–0.97
	P value	<0.001	<0.001	<0.001
	ICC	0.91	0.85	0.80
	95% CI	0.79–0.96	0.51–0.95	0.14–0.94
	P value	<0.001	<0.001	0.010
Plaque volume	*r*†	0.85	0.55	0.54
	95% CI	0.68–0.93	0.14–0.80	0.17–0.76
	P value	<0.001	0.013	0.005
	ICC	0.71	0.55	0.41
	95% CI	0.35–0.87	0.15–0.79	−0.01–0.70
	P value	<0.001	0.005	0.027

CI = confidence interval; ICC = intraclass correlation coefficient; *r* † = Pearson correlation coefficient; Software 1 = AutoSeg, AiMedic; Software 2 = Syngo.via, Siemens; Software 3 = IntelliSpace Portal, Philips

PCCs were similar for lumen volume in all three software platforms and software 1 showed the highest PCC for plaque volume (Table 3.1). ICC was the highest in software 1 for lumen and plaque volume (Table 3.1).

The Bland–Altman plots for lumen or plaque volume are shown in Figure 3.1.

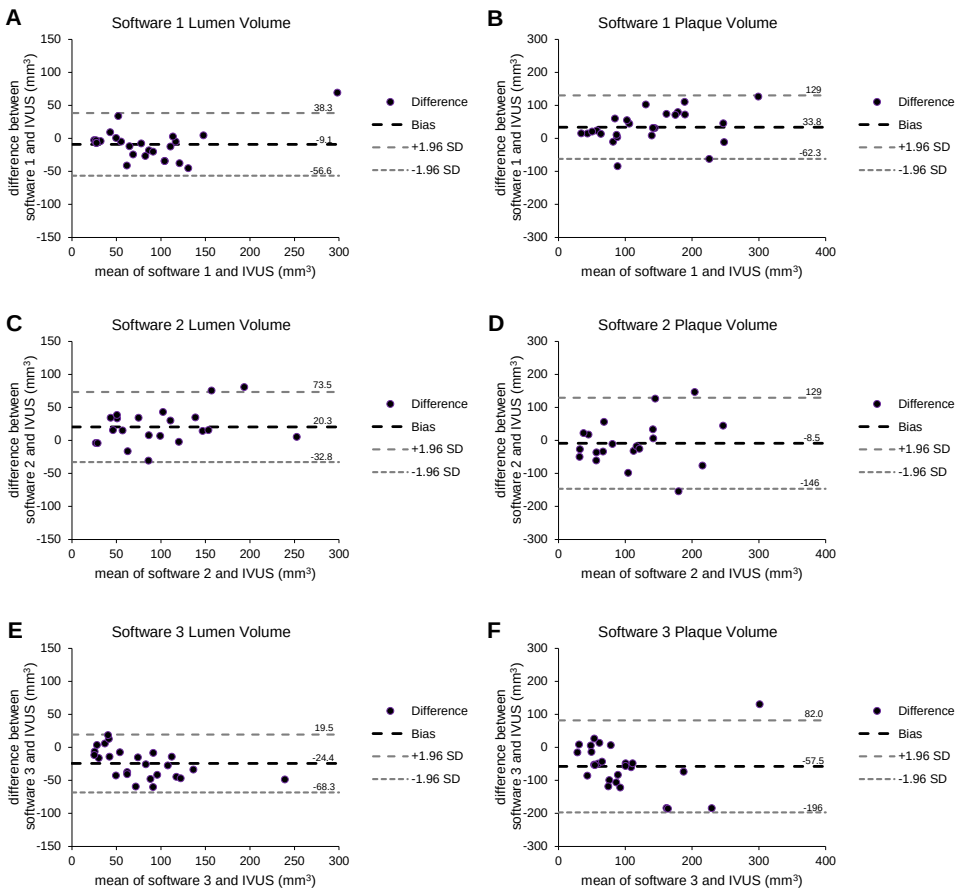

Figure 3.1. Bland-Altman plots of lumen or plaque volume measured by differences between each software platform and IVUS. (A-B) Bland-Altman plots of lumen (A) (mean difference = -9.1 mm^3, SD = 24.2 mm^3, 95% of CI of mean difference = -18.6 to 0.4 mm^3) or plaque volume (B) (mean difference = 33.8 mm^3, SD = 49.1 mm^3, 95% of CI of mean difference = 14.6 to 53.0 mm^3) measured by differences between software 1 and IVUS. (C-D) Bland-Altman plots of lumen (C) (mean difference = 20.3 mm^3, SD = 27.1 mm^3, 95% of CI of mean difference = 8.7 to 31.9 mm^3) or plaque volume

(D) (mean difference = −8.5 mm^3, SD = 70.3 mm^3, 95% of CI of mean difference = −39.3 to 22.3 mm^3) measured by differences between software 2 and IVUS. (E–F) Bland–Altman plots of lumen (E) (mean difference = −24.4 mm^3, SD = 22.4 mm^3, 95% of CI of mean difference = −33.2 to −15.6 mm^3) or plaque volume (F) (mean difference = −57.5 mm^3, SD = 71.1 mm^3, 95% of CI of mean difference = −84.7 to −30.1 mm^3) measured by differences between software 3 and IVUS. CI = confidence interval; SD = standard deviation; Software 1 = AutoSeg, AiMedic; Software 2 = Syngo.via, Siemens; Software 3 = IntelliSpace Portal, Philips

Software 1 showed the bias closest to zero for lumen volume (mean difference = −9.1 mm^3, SD = 24.2 mm^3, 95% of confidence interval [CI] of mean difference = −18.6 to 0.4 mm^3). Software 2 overestimated (mean difference = 20.3 mm^3, SD = 27.1 mm^3, 95% of CI of mean difference = 8.7 to 31.9 mm^3) and software 3 underestimated (mean difference = −24.4 mm^3, SD = 22.4 mm^3, 95% of CI of mean difference = −33.2 to −15.6 mm^3) lumen volume.

Moreover, software 2 showed the bias closest to zero for plaque volume (mean difference = −8.5 mm^3, SD = 70.3 mm^3, 95% of CI

of mean difference = −39.3 to 22.3 mm^3), but SD was the lowest in software 1 (mean difference = 33.8 mm^3, SD = 49.1 mm^3, 95% of CI of mean difference = 14.6 to 53.0 mm^3). Software 3 underestimated plaque volume with the highest SD (mean difference = −57.5 mm^3, SD = 71.1 mm^3, 95% of CI of mean difference = −84.7 to −30.1 mm^3).

3.2. Comparison of Lumen or Plaque Area for Three Different Software Platforms

To analyze the accuracy of lumen or plaque segmentation using different software platforms with sufficient number of sample size, the measured lumen or plaque area was compared with IVUS. The statistical analysis of PCC and ICC of lumen or plaque area for each software platform using IVUS data sets as gold standards is shown in Table 3.2 and Supplementary Figure S3.

Table 3.2. Pearson correlation coefficient and intraclass correlation coefficient of lumen or plaque area of each software platform based on IVUS data sets.

		Software 1	Software 2	Software 3
Lumen area	*r*†	0.79	0.75	0.76
	95% CI	0.77–0.80	0.73–0.78	0.73–0.78
	P value	<0.001	<0.001	<0.001
	ICC	0.76	0.71	0.61
	95% CI	0.66–0.82	0.58–0.80	0.19–0.79
	P value	<0.001	<0.001	0.003
Plaque area	*r*†	0.50	0.22	0.31
	95% CI	0.47–0.53	0.16–0.27	0.26–0.36
	P value	<0.001	<0.001	<0.001
	ICC	0.34	0.17	0.19
	95% CI	0.09–0.51	0.11–0.23	0.03–0.33
	P value	0.004	<0.001	0.009

CI = confidence interval; ICC = intraclass correlation coefficient; *r* † = Pearson correlation coefficient; Software 1 = AutoSeg, AiMedic; Software 2 = Syngo.via, Siemens; Software 3 = IntelliSpace Portal, Philips

For lumen area, PCCs were similar among different software platforms (Table 3.2). Software 1 showed the highest ICC with significant difference when compared with other software platforms (p = 0.005) (Table 3.3).

Table 3.3. Correlation coefficient comparison of each software platform based on intraclass correlation coefficient.

	ICC			ICC comparison (p-value)		
	S1 ICC	S2 ICC	S3 ICC	S1 vs. S2	S1 vs. S3	S2 vs. S3
Lumen volume	0.91 (0.79-0.96)	0.85 (0.51-0.95)	0.80 (0.14-0.94)	0.393	0.155	0.620
Plaque volume	0.71 (0.35-0.87)	0.55 (0.15-0.79)	0.41 (-0.01-0.70)	0.405	0.130	0.568
Lumen area	0.76 (0.66-0.82)	0.71 (0.58-0.80)	0.61 (0.19-0.79)	0.005	<0.001	<0.001
Plaque area	0.34 (0.09-0.51)	0.17 (0.11-0.23)	0.19 (0.03-0.33)	<0.001	<0.001	0.620
Lumen area in stenotic region	0.61 (0.56-0.65)	0.31 (0.00-0.53)	0.46 (0.33-0.56)	<0.001	<0.001	0.009
Lumen area in non-stenotic region	0.73 (0.47-0.84)	0.74 (0.67-0.78)	0.56 (-0.03-0.80)	0.654	<0.001	<0.001
Plaque area in stenotic region	0.36 (0.25-0.44)	0.15 (0.02-0.27)	0.16 (0.05-0.27)	<0.001	<0.001	0.885

Data represented in parentheses are 95% confidence interval; ICC = intraclass correlation coefficient; S1 = AutoSeg, AiMedic; S2 = Syngo.via, Siemens; S3 = IntelliSpace Portal, Philip

For plaque area, software 1 showed the highest PCC and ICC (Table 3.2). ICC of software 1 for plaque area was significantly higher than software 2 and 3 ($p < 0.001$) (Table 3.3).

The Bland-Altman plots for lumen or plaque area are shown in Figure 3.2.

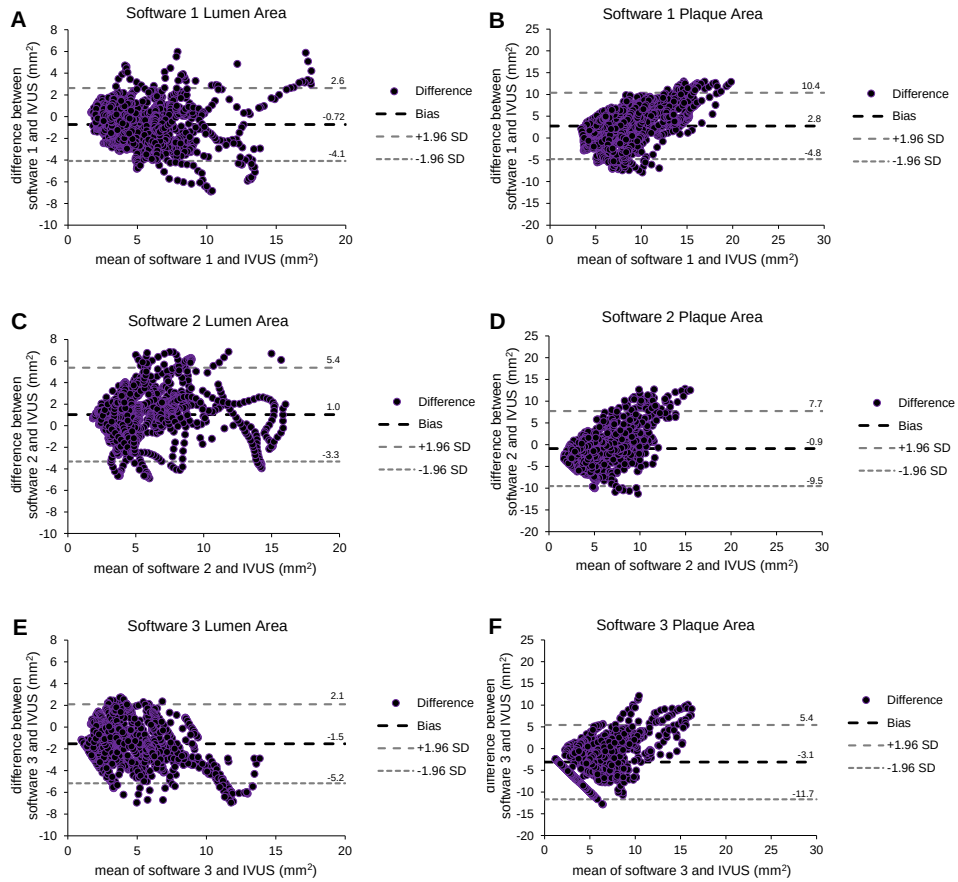

Figure 3.2. Bland-Altman plots of lumen or plaque area measured by differences between each software platform and IVUS. (A-B) Bland-Altman plots of lumen (A) (mean difference = −0.72 mm^2, SD = 1.71 mm^2, 95% of CI of mean difference = −0.80 to −0.64 mm^2) or plaque area (B) (mean difference = 2.76 mm^2, SD = 3.88 mm^2, 95% of CI of mean difference = 2.58 to 2.94 mm^2) measured by differences between software 1 and IVUS. (C-D) Bland-Altman plots of lumen (C) (mean difference = 1.03 mm^2, SD = 2.22 mm^2, 95% of CI of mean difference = 0.90 to 1.16 mm^2) or plaque area

(D) (mean difference = −0.90 mm^2, SD = 4.40 mm^2, 95% of CI of mean difference = −1.17 to −0.63 mm^2) measured by differences between software 2 and IVUS. (E–F) Bland–Altman plots of lumen (E) (mean difference = −1.54 mm^2, SD = 1.86 mm^2, 95% of CI of mean difference = −1.64 to −1.44 mm^2) or plaque area (F) (mean difference = −3.12 mm^2, SD = 4.37 mm^2, 95% of CI of mean difference = −3.36 to −2.88 mm^2) measured by differences between software 3 and IVUS. CI = confidence interval; SD = standard deviation; Software 1 = AutoSeg, AiMedic; Software 2 = Syngo.via, Siemens; Software 3 = IntelliSpace Portal, Philips

Software 1 showed the bias closest to zero for lumen area (mean difference = −0.72 mm^2, SD = 1.71 mm^2, 95% of CI of mean difference = −0.80 to −0.64 mm^2). Software 2 overestimated (mean difference = 1.03 mm^2, SD = 2.22 mm^2, 95% of CI of mean difference = 0.90 to 1.16 mm^2) and software 3 underestimated (mean difference = −1.54 mm^2, SD = 1.86 mm^2, 95% of CI of mean difference = −1.64 to −1.44 mm^2) lumen area.

Moreover, software 2 showed the bias closest to zero for plaque area (mean difference = −0.90 mm^2, SD = 4.40 mm^2, 95% of CI of mean difference = −1.17 to −0.63 mm^2), but SD was the lowest in

software 1 (mean difference = 2.76 mm^2, SD = 3.88 mm^2, 95% of CI of mean difference = 2.58 to 2.94 mm^2). Software 3 underestimated plaque area (mean difference = −3.12 mm^2, SD = 4.37 mm^2, 95% of CI of mean difference = −3.36 to −2.88 mm^2).

3.3. Subgroup Lumen Area Analysis in Stenotic and Non-Stenotic Region

To determine the stenosis severity of lumen for diagnosing CAD, the accuracy of detecting lumen area for both stenotic and non-stenotic regions is important. Therefore, the measured lumen area in stenotic or non-stenotic region using different software platforms was compared with IVUS. The statistical analysis of PCC and ICC of lumen area in stenotic or non-stenotic region for each software platform using IVUS data sets as gold standards is shown in Table 3.4 and Supplementary Figure S4.

Table 3.4. Pearson correlation coefficient and intraclass correlation coefficient of lumen area in stenotic or non-stenotic region of each software platform based on IVUS data sets.

		Software 1	Software 2	Software 3
Lumen area in stenotic region	*r*†	0.62	0.52	0.50
	95% CI	0.57–0.66	0.44–0.59	0.43–0.56
	P value	<0.001	<0.001	<0.001
	ICC	0.61	0.31	0.46
	95% CI	0.56–0.65	0.00–0.53	0.33–0.56
	P value	<0.001	0.025	<0.001
Lumen area in non–stenotic region	*r*†	0.79	0.75	0.78
	95% CI	0.77–0.82	0.72–0.78	0.75–0.80
	P value	<0.001	<0.001	<0.001
	ICC	0.73	0.74	0.56
	95% CI	0.47–0.84	0.67–0.78	−0.03–0.80
	P value	<0.001	<0.001	0.034

CI = confidence interval; ICC = intraclass correlation coefficient; *r* † = Pearson correlation coefficient; Software 1 = AutoSeg, AiMedic; Software 2 = Syngo.via, Siemens; Software 3 = IntelliSpace Portal, Philips

For lumen area in stenotic region, software 1 showed the highest PCC and ICC (Table 3.4). ICC of software 1 was significantly higher than software 2 and 3 for lumen area in stenotic region ($p < 0.001$) (Table 3.3).

For lumen area in non–stenotic region, PCCs were similar among different software platforms (Table 3.4). Software 1 and 2 showed similar ICCs and software 3 showed the lowest ICC (Table 3.4).

Moreover, ICCs of software 1 and 2 for lumen area in non-stenotic region were significantly higher than software 3 ($p < 0.001$) (Table 3.3).

The Bland-Altman plots for lumen area in stenotic or non-stenotic region are shown in Figure 3.3.

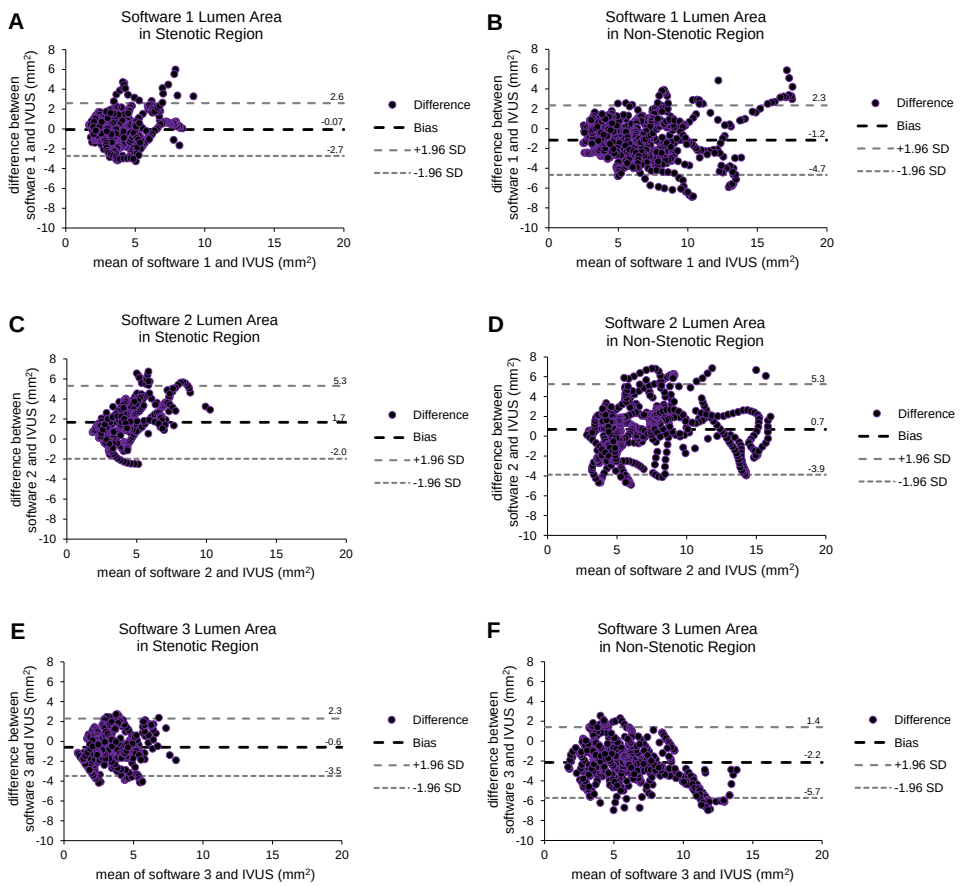

Figure 3.3. Bland-Altman plots of lumen area in stenotic or non-stenotic region measured by differences between each software

platform and IVUS. (A–B) Bland–Altman plots of lumen area in stenotic (A) (mean difference = −0.07 mm^2, SD = 1.36 mm^2, 95% of CI of mean difference = −0.16 to 0.02 mm^2) or non–stenotic region (B) (mean difference = −1.16 mm^2, SD = 1.79 mm^2, 95% of CI of mean difference = −1.26 to −1.06 mm^2) measured by differences between software 1 and IVUS. (C–D) Bland–Altman plots of lumen area in stenotic (C) (mean difference = 1.66 mm^2, SD = 1.86 mm^2, 95% of CI of mean difference = 1.48 to 1.84 mm^2) or non–stenotic region (D) (mean difference = 0.69 mm^2, SD = 2.33 mm^2, 95% of CI of mean difference = 0.52 to 0.86 mm^2) measured by differences between software 2 and IVUS. (E–F) Bland–Altman plots of lumen area in stenotic (E) (mean difference = −0.59 mm^2, SD = 1.47 mm^2, 95% of CI of mean difference = −0.72 to −0.46 mm^2) or non–stenotic region (F) (mean difference = −2.15 mm^2, SD = 1.82 mm^2, 95% of CI of mean difference = −2.28 to −2.02 mm^2) measured by differences between software 3 and IVUS. CI = confidence interval; SD = standard deviation; Software 1 = AutoSeg, AiMedic; Software 2 = Syngo.via, Siemens; Software 3 = IntelliSpace Portal, Philips

Software 1 showed the bias closest to zero and the lowest SD for

lumen area in stenotic region (mean difference = −0.07 mm^2, SD = 1.36 mm^2, 95% of CI of mean difference = −0.16 to 0.02 mm^2). In stenotic region, software 2 overestimated (mean difference = 1.66 mm^2, SD = 1.86 mm^2, 95% of CI of mean difference = 1.48 to 1.84 mm^2) and software 3 underestimated (mean difference = −0.59 mm^2, SD = 1.47 mm^2, 95% of CI of mean difference = −0.72 to −0.46 mm^2) lumen area.

Moreover, software 2 showed the bias closest to zero for lumen area in non−stenotic region (mean difference = 0.69 mm^2, SD = 2.33 mm^2, 95% of CI of mean difference = 0.52 to 0.86 mm^2), but SD was the lowest in software 1 (mean difference = −1.16 mm^2, SD = 1.79 mm^2, 95% of CI of mean difference = −1.26 to −1.06 mm^2). Software 3 underestimated lumen area in non−stenotic region (mean difference = −2.15 mm^2, SD = 1.82 mm^2, 95% of CI of mean difference = −2.28 to −2.02 mm^2).

3.4. Subgroup Plaque Area Analysis in Stenotic Region

To evaluate CAD, accuracy of detecting the amount of lipid or calcium in the vessel of coronary artery is important. The stenotic region with high plaque burden (see Materials and Methods) was

used for the analysis, and the measured plaque area in stenotic region using different software platforms was compared with IVUS. The statistical analysis of PCC and ICC of plaque area in the stenotic region for each software platform using IVUS data sets as gold standards is shown in Table 3.5 and Supplementary Figure S5.

Table 3.5. Pearson correlation coefficient and intraclass correlation coefficient of plaque area in stenotic region of each software platform based on IVUS data sets.

		Software 1	Software 2	Software 3
Plaque area in stenotic region	*r*†	0.52	0.24	0.27
	95% CI	0.47–0.58	0.13–0.33	0.19–0.35
	P value	<0.001	<0.001	<0.001
	ICC	0.36	0.15	0.16
	95% CI	0.25–0.44	0.02–0.27	0.05–0.27
	P value	<0.001	0.012	0.002

CI = confidence interval; ICC = intraclass correlation coefficient; *r* † = Pearson correlation coefficient; Software 1 = AutoSeg, AiMedic; Software 2 = Syngo.via, Siemens; Software 3 = IntelliSpace Portal, Philips

PCC was the highest in software 1 for plaque area in stenotic region (Table 3.5). Moreover, ICCs showed similar tendency to

PCCs for plaque area in stenotic region with the highest ICC for software 1 (Table 3.5). ICC of software 1 for plaque area in stenotic region was significantly higher than software 2 and 3 ($p < 0.001$) (Table 3.3).

The Bland-Altman plots for plaque area in stenotic region are shown in Figure 3.4.

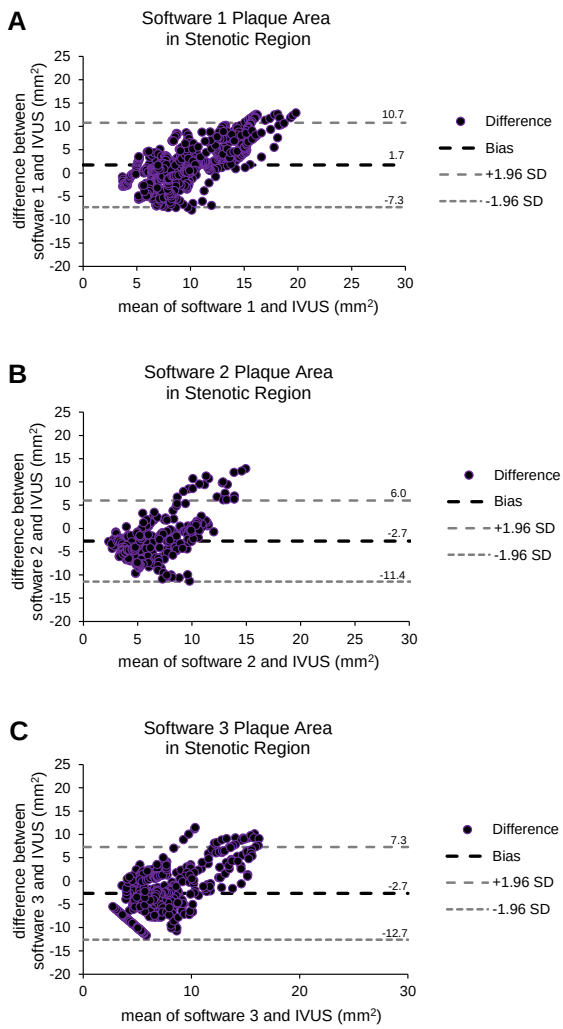

Figure 3.4. Bland-Altman plots of plaque area in stenotic region measured by differences between each software platform and IVUS. (A) Bland-Altman plots of plaque area in stenotic region (mean difference =1.70 mm^2, SD = 4.61 mm^2, 95% of CI of mean difference = 1.37 to 2.03 mm^2) measured by differences between software 1 and IVUS. (B) Bland-Altman plots of plaque area in stenotic region (mean difference = −2.72 mm^2, SD = 4.45 mm^2, 95% of CI of mean difference = −3.20 to −2.24 mm^2) measured by differences between software 2 and IVUS. (C) Bland-Altman plots of plaque area in stenotic region (mean difference = −2.67 mm^2, SD = 5.08 mm^2, 95% of CI of mean difference = −3.11 to −2.23 mm^2) measured by differences between software 3 and IVUS. CI = confidence interval; SD = standard deviation; Software 1 = AutoSeg, AiMedic; Software 2 = Syngo.via, Siemens; Software 3 = IntelliSpace Portal, Philips

The bias was the lowest for plaque area in stenotic region of software 1 (mean difference =1.70 mm^2, SD = 4.61 mm^2, 95% of CI of mean difference = 1.37 to 2.03 mm^2). Software 2 (mean difference = −2.72 mm^2, SD = 4.45 mm^2, 95% of CI of mean difference = −3.20 to −2.24 mm^2) and software 3 (mean difference

= −2.67 mm^2, SD = 5.08 mm^2, 95% of CI of mean difference = −3.11 to −2.23 mm^2) underestimated plaque area in stenotic region.

Chapter 4. Conclusion and Future Works

CAD is the leading problem of mortality in the world inducing various complications related to cardiovascular system (1-4). CCTA is widely used to evaluate CAD, which is a well-known method for non-invasive evaluation for disease diagnosis (5-8). An automatic segmentation of coronary arteries using CCTA images can be performed in several commercially available software platforms and analyses related to the CAD are possible (9, 10).

However, there is no study which compared both lumen and plaque parameters for several software platforms using CCTA images. To this end, this study analyzed a newly developed software platform with NLATM (software 1) with commercially available software platforms using IVUS data sets as gold standards. The performance of the segmentation algorithm of three software platforms was compared using the data set of lumen or plaque parameters at a fixed interval for a certain length of the target segments. Statistical analyses such as PCC, ICC, and Bland-Altman plot were conducted using lumen or plaque parameters (volume and area) by comparing the data of each software platform with those of IVUS. Analysis of software platform segmenting coronary arteries led to the following conclusions: (i) PCC and ICC were the highest

with the bias closest to zero for lumen volume (PCC = 0.92, 95% CI = 0.83 to 0.97; ICC = 0.91, 95% CI = 0.79 to 0.96; mean difference = −9.1 mm^3, 95% CI = −18.6 to 0.4 mm^3) or area (PCC = 0.79, 95% CI = 0.77 to 0.80; ICC = 0.76, 95% CI = 0.66 to 0.82; mean difference = −0.72 mm^2, 95% CI = −0.80 to −0.64 mm^2) when compared software 1 with IVUS. (ii) PCC and ICC were the highest and the bias was closest to zero for lumen (PCC = 0.62, 95% CI = 0.57 to 0.66; ICC = 0.61, 95% CI = 0.56 to 0.65; mean difference = −0.07 mm^2, 95% CI = −0.16 to 0.02 mm^2) or plaque area (PCC = 0.52, 95% CI = 0.47 to 0.58; ICC = 0.36, 95% CI = 0.25 to 0.44; mean difference = 1.70 mm^2, 95% CI = 1.37 to 2.03 mm^2) in the stenotic region when compared software 1 with IVUS. (iii) The performance of detecting lumen or plaque area in stenotic region was the best in software 1 when compared with other software platforms ($p < 0.001$).

Stenosis severity of lumen or assessment of plaque composition is an important issue for evaluating CAD in the clinical field (33). For software platforms which use CCTA images as inputs, an automatic segmentation of coronary arteries can assist analyses related to the CAD. To analyze CAD with higher efficiency using software platforms, the accuracy of detecting coronary lumen or

plaque parameters in stenotic region is an essential factor. Based on the result of the study, software 1 showed significantly outstanding performance in detecting lumen or plaque area in stenotic region when compared with other software platforms based on IVUS data as gold standards. This result implies that the newly developed software 1 has a potential in assisting evaluation of CAD.

For all software platforms, the performance of detecting lumen area showed higher accuracy when compared with plaque area because the outer wall is generally more challenging than lumen. To assist CAD using plaque composition, there is a need for improvement of algorithms detecting plaque area. Especially, software 2 showed extremely high plaque area in some spots where coronary arteries are located near the chambers or veins with the failure rate of 7% (Supplementary Figure S6 and Table S1). In contrast, software 3 showed extremely low plaque area in some non-stenotic regions (Figure 2.2F). Software 1 showed overestimated tendency for plaque volume calculation (Figure 3.1B), but showed the lowest bias of 1.7 mm^2 for plaque area in stenotic region when compared with other software platforms (Figure 3.4). For lumen area in stenotic region, software 1 showed the outstanding performance with the bias of -0.07 mm^2. PCC and ICC

were also the highest for software 1 which showed the potential of NLATM in aiding CAD using the accurate segmentation of coronary arteries in stenotic region (Figure 3.3A).

The limitation of this study was the inconsistency between software platforms. The lumen or plaque area was compared with IVUS data sets using the cross-sectional planes of the centerline for three software platforms. The interval of IVUS data sets and three software platforms were 0.001 mm and 0.2-0.5 mm, respectively. Due to the interval difference among software platforms, the interval of IVUS data was modified adaptively according to each software platform for the area comparison. This situation may have led to an inaccurate comparison of lumen or plaque area among software platforms. Moreover, the starting points and cross-sectional planes of the centerline in IVUS data do not always overlap accurately with CT images leading to the length misalignment (34). This situation may cause the low PCC and ICC for three software platforms when compared with IVUS data.

In addition to this study, the validation of plaque composition and an automatic calculating algorithm for stenosis degree using software 1 is possible in the near future. This study validated the plaque area, but not the plaque composition such as calcium, lipid,

fibrous, fibro-fatty, or necrotic core. Visualization of plaque composition in software 1 may help the analysis and evaluation of the CAD. Moreover, automatic calculation of stenosis degree is possible using the lumen area of a certain vessel. This technique may help diagnosing CAD when an expert evaluation is not available.

Measurement of fractional flow reserve (FFR) is widely used for evaluating CAD (35, 36). CAD patients with FFR of 0.8 or less are recommended for stent implantation due to the capability of inducing ischemia (36, 37). However, an invasive procedure is required to measure FFR (38). CCTA-derived FFR (CT-FFR) is an alternative technique used for CAD diagnosis which is a non-invasive method (39-44). The generated 3D model of coronary arteries from software 1 could be applied for the analysis of CT-FFR to assist diagnosing CAD.

In summary, the performance of the segmentation algorithm of commercially available software platforms was analyzed using the data sets of coronary lumen or plaque parameters from IVUS as gold standards. The statistical analysis showed that software platform with NLATM was the best for detecting lumen or plaque area in the stenotic region. This study suggests the newly developed software platform with NLATM as an aiding system for

diagnosing CAD.

Part 2. Analysis of blooming artifact from calcification using computed tomography

Chapter 5. Introduction

Coronary artery disease (CAD) is a major cause of death worldwide and is known as one of the serious health problems, which can induce various risks related to the heart and blood vessels (1, 3, 4). Therefore, many researches are currently focusing on treatment and prevention of CAD (1). Computed tomography (CT) is widely used for non-invasive evaluation of CAD (5-8). Conventional CT uses a polychromatic beam which consists of a wide spectrum of photon energy and polychromatic images are reconstructed (45). In contrast to conventional CT, dual-energy CT (DECT) uses a monochromatic beam which synthesizes a virtual monochromatic image with obtained polychromatic images and has an advantage in dual absorption or emission of photons using different energy levels which can decompose the tissues into distinguished components (46-49). However, blooming artifact can be observed in CT images for patient with a high level of coronary artery calcium when compared with coronary angiography images (50-53). This situation leads to

the underestimation of the actual vessel size when evaluating the stenosis degree of coronary arteries (50-53).

Previous researches were conducted to find out the strategies for reducing blooming artifact from calcification on CT images and suggested increasing X-ray energy levels such as kilovoltage peak (kVp) in conventional polychromatic images or kilo-electron volts (keV) in virtual monochromatic images with subjective visual assessment (54-57). Higher X-ray energy levels decrease attenuation values on calcification in CT images which also can be produced by increasing the width of window. We hypothesized that higher X-ray energy levels may decrease blooming artifact from calcification with subjective visual assessment in CT images, but fail to reduce adjacent affected pixel from calcification with objective quantitative measurement. This research has been conducted to quantitatively analyze the effect of higher X-ray energy levels on measurement of adjacent affected pixel from calcification through a phantom study.

To this end, a phantom was designed considering various shapes and sizes of calcium. The designed phantom was manufactured by a three-dimensional (3D) printer. The manufactured phantom was completely filled with a mixture of calcium phosphate powder and

droplets of distilled water. Polychromatic and virtual monochromatic images of the manufactured phantom were acquired by changing X-ray energy levels using commercially available DECT scanners (Siemens [vendor 1], Philips [vendor 2], and GE [vendor 3]) which use different implementation methods such as radiation dose, separation and registration (58). Adjacent affected pixel from calcification was calculated by subtracting the brightened region from the actual calcified region. Full width at third maximum (FWTM) was used to determine the actual calcified region because it showed the error of calculating the calcified region close to zero (mean error = 0.05 mm and standard error of mean [S.E.M] = 0.01 mm). Objective quantitative measurement of adjacent affected pixel from calcification was analyzed using the distance of the brightened region excluding the actual calcified region determined by FWTM. By analyzing adjacent affected pixel from calcification using different X-ray energy levels, we found that the change in kVp levels in polychromatic images did not show the reduction of adjacent affected pixel from calcification (Field of view [FOV] 300 mm, p = 0.167, 0.494, and 0.861; FOV 150 mm, p = 0.150, 0.161, and 0.075 for vendor 1, 2, and 3). Moreover, adjacent affected pixel from calcification showed different aspects according to keV levels

for virtual monochromatic images obtained from three implementation methods of DECT (FOV 300 mm, no significant difference [p = 0.191], increase [p < 0.001], and decrease [p <0.001] for vendor 1, 2, and 3). The results indicate that increasing X-ray energy levels such as kVp or keV reduces blooming artifact from calcification with subjective visual assessment, but induces no significant difference of adjacent affected pixel from calcification with objective quantitative measurement.

Chapter 6. Materials and Methods

6.1. Phantom Design

To investigate adjacent affected pixel from calcification with objective quantitative measurement, a phantom was designed using Solidworks software (Dassault Systemes) considering various geometric differences such as size, shape, or degree of calcification (Figure 6.1).

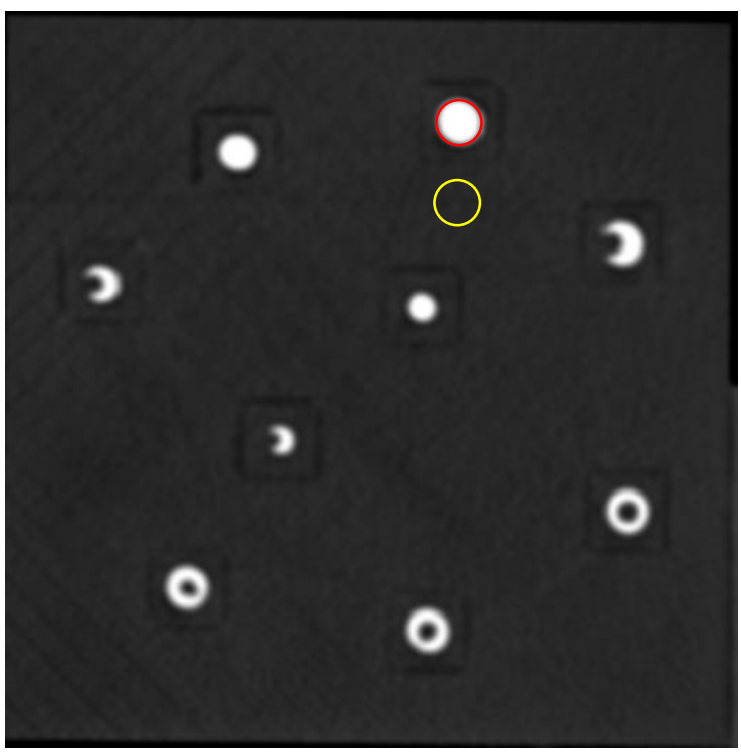

Figure 6.1. A reconstructed computed tomography image using a

phantom. A reconstructed computed tomography image of a phantom. The size, shape, and degree of calcification are different for each component comprising the phantom. Red and yellow lines indicate the region of interest (ROI) and the background region, respectively. Contrast to noise ratio, signal to noise ratio, and noise were calculated using the selected ROI and the background region.

The final phantom was manufactured with acrylonitrile–butadiene–styrene (ABS) using a 3D printer (3DWOX 2X, Sindoh) and was completely filled with a mixture of calcium phosphate powder and droplets of distilled water. When filling the calcium mixture into the manufactured phantom, a sharp tool was used to remove air bubbles through several small holes at the bottom of the phantom. Moreover, a compression tool was used so that the calcium mixture could be compactly filled.

6.2. Computed Tomography Protocols and Reconstruction

All CT scans were performed in helical scan using an abdomen protocol for five times on different dates from June 22, 2022, to August 9, 2022, at Seoul National University Hospital using three

different DECT scanners (SOMATOM Force, Siemens [vendor 1]; IQon – Spectral CT, Philips [vendor 2]; Revolution Apex, GE [vendor 3]). Conventional polychromatic scans were done using three different CT scanners at 80, 100, 120, 140 kVp in different FOVs (large FOV: 300 mm, small FOV: 150 mm) for analyzing adjacent affected pixel from calcification according to the X-ray energy difference. The tube current was adjusted at 250 mA for each vendor except for the virtual monochromatic images for vendor 2 because it used two tubes for scanning (240 mA for 80 kv and 120 mA for 140 kv). Rotation times of 330 – 1000 ms, collimation of 192 * 0.6 mm / 128 * 0.6 mm / 16 * 0.625 / 40 * 0.625, pitch of 0.6 – 0.984 were used for scanning parameters for different vendors (Supplementary Table S3). CT images were reconstructed using a unique algorithm for each vendor with slice thickness of 0.6 – 0.8 mm (Supplementary Table S3). Virtual monochromatic scans were performed for each DECT vendor using different implementation methods ([a] SOMATOM Force, Siemens; dual independent source with detector, [b] IQon – Spectral CT, Philips; single source and dual layer detector, [c] Revolution Apex, GE; single source with detector using rapid tube potential switching). Virtual monochromatic reconstruction was done at 40,

70, 100, 130, and140 keV through each proved software (Syngo.via, Siemens; IntelliSpace Portal, Philips; A/W server 2, GE).

6.3. Measurement of Distortion Angle of a Phantom

For accurate calculation of adjacent affected pixel from calcification, the distortion angle of the phantom was measured for each scan using different vendors (Table 6.1 and Supplementary Figure S7). The distortion angle was measured in degrees for anterior or left view of the reconstructed 3D images of the phantom through Rapidia 3D version 2.8 (INFINITT Co., Ltd.). The distortion angle in axial view was calculated using the equation as follows:

$$Distortion\ angle\ (degrees) = \frac{180}{\pi} \times arctan\sqrt{(tan\theta_1)^2 + (tan\theta_2)^2}$$

where θ_1 and θ_2 are the distortion angles in anterior and left view, respectively. The measurement error according to the distortion angle was calculated using the equation as follows:

$$Measurement\ error\ (\%) = \left(1 - \frac{1}{\cos\theta}\right) \times 100$$

where θ is the calculated distortion angle.

Table 6.1. Distortion angles of CT images using a phantom.

		Scan 1	Scan 2	Scan 3	Scan 4	Scan 5
Distortion angle (degrees)	Vendor 1	1.56	1.40	1.01	1.40	1.16
	Vendor 2	1.42	2.06	1.23	0.76	1.22
	Vendor 3	1.03	1.87	1.32	0.92	0.75
Measurement error (%)	Vendor 1	0.04	0.03	0.02	0.03	0.02
	Vendor 2	0.03	0.06	0.02	0.01	0.02
	Vendor 3	0.02	0.05	0.03	0.01	0.01

Distortion angles of CT images obtained from five repetitive scans for each vendor. Vendor 1 = Siemens; Vendor 2 = Philips; Vendor 3 = GE

6.4. Measurement of Contrast to Noise Ratio, Signal to Noise Ratio, and Noise

To validate the quality of CT images of a phantom, contrast to noise ratio (CNR), signal to noise ratio (SNR), and noise were calculated for polychromatic and virtual monochromatic images using each vendor. The region of interest (ROI) was set as the calcium region with the diameter of 6 mm and the background region was located at the lower part of ROI (Figure 6.1). CNR was defined as difference of the average Hounsfield unit (HU) in the ROI and the background region divided by SD of HU in the background region. SNR was defined as the average HU of ROI divided by SD of HU in the background region. Noise was defined as SD of HU in the background region. Data are represented as mean

value and S.E.M (Table 6.2). All calculations were conducted using Matlab® .

Table 6.2. Contrast to noise ratio, signal to noise ratio, and noise calculated for polychromatic and virtual monochromatic images of a phantom using each vendor.

			Computed tomography quality parameters			
	Image type	X-ray energy	CNR	SNR	Noise	Maximum HU
Vendor 1	Polychromatic	80	95.10 ± 4.91	93.57 ± 4.90	12.10 ± 0.59	2276 ± 24
		100	85.81 ± 3.49	84.71 ± 3.38	10.94 ± 0.42	1873 ± 19
		120	79.10 ± 4.19	78.79 ± 4.11	10.41 ± 0.48	1645 ± 18
		140	82.23 ± 5.31	81.82 ± 5.27	9.17 ± 0.50	1505 ± 15
	Virtual mono-chromatic	40	110.43 ± 5.39	108.81 ± 5.33	15.41 ± 0.80	3071 ± 0
		70	96.68 ± 4.65	95.44 ± 4.59	7.33 ± 0.28	1404 ± 13
		100	56.09 ± 2.64	55.34 ± 2.62	7.73 ± 0.35	871 ± 9
		130	41.40 ± 2.04	40.83 ± 1.98	8.14 ± 0.41	687 ± 8
		140	38.84 ± 1.98	38.30 ± 1.90	8.23 ± 0.42	654 ± 8
Vendor 2	Polychromatic	80	122.87 ± 5.21	121.61 ± 5.18	9.72 ± 0.36	2404 ± 5
		100	109.11 ± 4.96	109.01 ± 4.96	9.05 ± 0.33	1994 ± 6
		120	87.86 ± 2.97	88.36 ± 2.98	9.75 ± 0.27	1744 ± 6
		140	77.52 ± 3.27	78.41 ± 3.29	10.00 ± 0.40	1568 ± 5
	Virtual mono-chromatic	40	203.22 ± 3.52	199.38 ± 3.23	8.80 ± 0.69	3071 ± 0
		70	115.81 ± 5.40	117.46 ± 5.44	6.40 ± 0.31	1493 ± 12
		100	74.60 ± 3.54	78.00 ± 3.68	6.21 ± 0.30	954 ± 10
		130	60.07 ± 3.04	64.07 ± 3.22	6.17 ± 0.32	772 ± 9
		140	57.57 ± 2.98	61.69 ± 3.18	6.15 ± 0.33	739 ± 9
Vendor 3	Polychromatic	80	54.68 ± 2.31	53.09 ± 2.29	18.01 ± 0.63	1976 ± 8
		100	62.15 ± 1.77	60.73 ± 1.80	12.90 ± 0.24	1617 ± 6
		120	64.66 ± 3.84	63.39 ± 3.83	11.05 ± 0.46	1418 ± 6
		140	63.05 ± 2.50	61.87 ± 2.63	10.12 ± 0.26	1274 ± 7
	Virtual mono-chromatic	40	71.45 ± 3.21	69.43 ± 3.11	24.54 ± 0.93	3071 ± 0
		70	65.51 ± 3.11	64.52 ± 3.03	11.69 ± 0.45	1498 ± 11
		100	56.27 ± 2.69	56.08 ± 2.64	8.39 ± 0.32	946 ± 6
		130	50.86 ± 2.42	51.11 ± 2.39	7.29 ± 0.28	758 ± 5
		140	49.62 ± 2.33	49.98 ± 2.31	7.08 ± 0.26	723 ± 5
P-value	Polychromatic	kVp levels	0.615	0.801	0.801	0.029
	Virtual mono-chromatic	keV levels	0.017	0.017	0.155	0.017

CNR = contrast to noise ratio; HU = Hounsfield unit; keV = kilo-electron volts; kVp = kilovoltage peak; SNR = signal to noise ratio; Vendor 1 = Siemens; Vendor 2 = Philips; Vendor 3 = GE; Data are represented as mean ± S.E.M of results. Friedman test was used for the calculation of p-value for comparing the quality of computed tomography image among different X-ray energy levels.

6.5. Measurement of Adjacent Affected Pixel from Calcification

Adjacent affected pixel from calcification was defined as the brightened region excluding the actual calcified region. The actual calcified region was determined using the definition of full width at third maximum (FWTM) instead of full width a half maximum (FWHM) which is a widely used measurement method (59). A third or half maximum attenuation value of the calcified region with the background value of zero was used for measuring FWTM or FWHM, respectively. Different sizes of calcification with concentric shape were used for the FWTM or FWHM measurement and the mean error against the real diameter was calculated (mean error = 0.05 and 0.47 mm using FWTM and FWHM, respectively) (Figure 6.2).

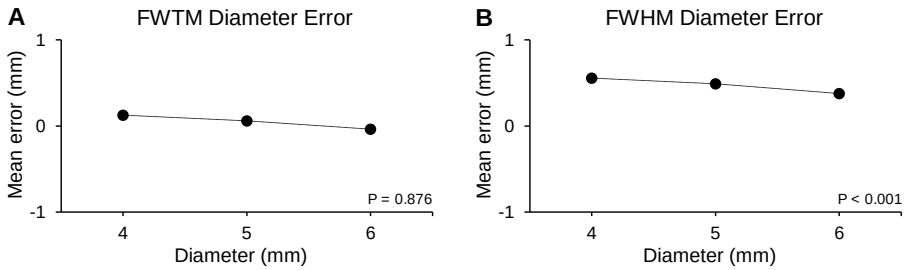

Figure 6.2. Graph plots of diameter error when using full width at third or half maximum. (A–B) Graph plots of diameter error of full width at third maximum (mean error = 0.05 mm; S.E.M = 0.01 mm) (A) or full width at half maximum (mean error = 0.47 mm; S.E.M = 0.01 mm) (B) using different sizes of calcification with concentric shape. FWHM = full width at half maximum; FWTM = full width at third maximum; Data are represented as mean ± S.E.M of results. Wilcoxon signed–rank test was used for the calculation of p–value comparing with the reference error of 0.04 mm.

The brightened region except the actual calcified region was defined as the adjacent affected pixel from calcification. The maximum and minimum thresholds of the brightened region were set as the attenuation value located at the edge of FWTM and 5% to the highest brightness of calcified region, respectively (Supplementary Figure S8). Adjacent affected pixel of each calcified shape was calculated by average pixel spacing of

brightened regions using four different directions (top, bottom, left, and right). Adjacent affected pixel was calculated for CT images obtained from five repetitive scans. All calculations were conducted using Matlab® .

6.6. Statistical Analysis

The measured adjacent affected pixel from calcification was investigated through the non-parametric tests for analyzing effects of different FOVs, sizes, shapes, kVp, or keV levels using CT images. All statistical analyses were performed using the median value obtained from five repetitive CT scans. Wilcoxon signed-rank test was used for comparing (i) mean error for estimating real calcified region using FWHM or FWTM with the reference of 0.04 mm, (ii) adjacent affected pixel for different FOVs, shapes or vendors (iii) adjacent affected pixel in virtual monochromatic images with the reference of low or high kVp levels in polychromatic images (60). Friedman test was used for comparing (i) CT image quality among different kVp or keV levels using CNR, SNR, and noise, (ii) adjacent affected pixel of different kVp or keV levels, sizes, and degrees using tube shape calcification (61). For plotting adjacent affected pixel using different kVp or keV levels,

the mean value and S.E.M calculated for each shape with different geometries (n = 9) were used. Moreover, for plotting adjacent affected pixel to compare different sizes, shapes, or degrees of calcification, the mean value and S.E.M calculated for kVp and keV levels of each FOV (n = 9) were used. A p-value less than 0.05 was considered statistically significant. All analyses were conducted using software, R version 4.2.0 package.

Chapter 7. Results

7.1. Acquirement of Reconstructed Computed Tomography Images Using a Phantom

To quantitatively investigate the relationship between adjacent affected pixel from calcification and different X-ray energy levels such as kVp or keV using various vendors, polychromatic and virtual monochromatic CT images of a phantom were acquired (Figure 6.1, see Materials and Methods). For accurate calculation of adjacent affected pixel from calcification, the distortion angle of the phantom was measured (see Materials and Methods). The result showed the distortion angle with maximum of 2.06 degrees (mean distortion angle = 1.27 degrees with SD of 0.37) and the measurement error with maximum of 0.06% (mean measurement error = 0.03% with SD of 0.01). Due to the low measurement error in distortion angle of the phantom, the reconstructed images with axial position were used for the analysis of adjacent affected pixel from calcification (Table 6.1 and Supplementary Figure S7).

Moreover, CT quality was validated through CNR, SNR, and noise (Figure 6.1, see Materials and Methods). Each value represented the quality of the reconstructed images of each DECT scanner

(Table 6.2). CNR was similar to SNR because the attenuation values of background were close to zero. CNR, SNR, and noise showed no significant difference among kVp levels in polychromatic images ($p = 0.615$, 0.801 and 0.801 for CNR, SNR, and noise). However, CNR and SNR excluding noise showed significant difference among keV levels in virtual monochromatic images due to the exponential decrease of maximum value of Hounsfield unit (HU) along the higher keV levels ($p = 0.017$, 0.017, and 0.155 for CNR, SNR, and noise). Importantly, the maximum HU of calcification was significantly different among kVp ($p = 0.029$) or keV ($p = 0.017$) levels with decreasing attenuation values along the higher X-ray energy levels.

7.2. Subjective Visual Assessment of Blooming Artifact

After the validation of the CT quality, the blooming artifact in CT images was subjectively observed using different window widths or kVp levels with visual assessment. Higher kVp levels decreased attenuation values of calcification which induced the reduction of blooming artifact with subjective visual assessment (Figure 7.1A

and B). Moreover, increasing window width of reconstructed images with lower kVp levels showed similar visual assessment of blooming effect with the image of the highest kVp level (Figure 7.1C and D).

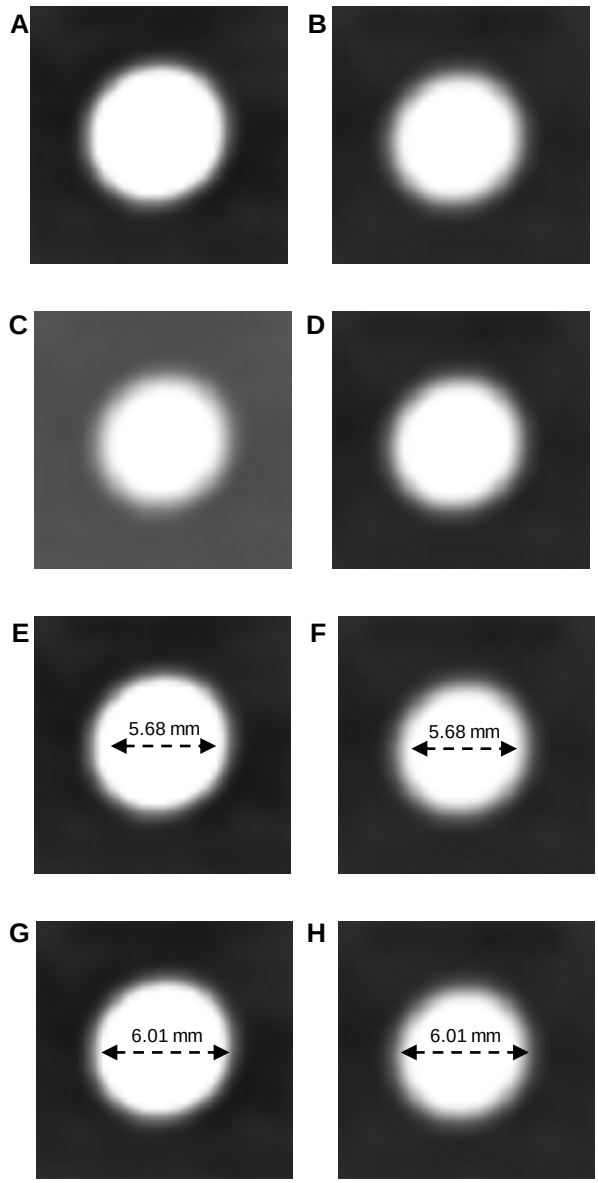

Figure 7.1. Computed tomography images of a phantom using different kilovoltage peak levels and window widths with quantitative

measurement. Images of a concentric shape of calcification with diameter of 6 mm scanned with kilovoltage peak level of 80 (A, C, E and G) or 140 (B, D, F, and H). The window center is fixed at 500 with width of 3000 (C), or 1500 (A–B and D–H). (E–H) Diameter calculated using full width at half maximum (5.68 mm) (E and F) or full width at third maximum (6.01 mm) (G and H) using a representative computed tomography image of the phantom.

This result showed that subjective visual assessment of blooming artifact is dependent on X-ray energy levels as well as the window width of CT images.

7.3. Objective Quantitative Measurement of Adjacent Affected Pixel from Calcification

After the observation of subjective visual assessment of blooming artifact, adjacent affected pixel from calcification was quantitatively measured for reconstructed images using each DECT vendor to validate the relationship with higher or lower X-ray energy levels. Adjacent affected pixel from calcification was calculated by subtracting the brightened region from the actual calcified region (Supplementary Figure S8, see Materials and Methods). To

determine the actual calcified region, FWHM was measured for each kVp or keV level and it showed consistency regardless of different attenuation values from calcification (Figure 7.1E and F). However, FWTM measured the actual calcified region with the mean error less than FWHM (Figure 7.1G and H). Moreover, the mean error using FWTM showed no significant difference when compared with the reference error of 0.04 mm (mean error = 0.05 mm, S.E.M = 0.01 mm, and $p = 0.876$) (Figure 6.2A). Mean error for measuring the actual calcified region using FWHM was 0.47 mm and showed significant difference when compared with the reference error of 0.04 mm (mean error = 0.47 mm, S.E.M = 0.01 mm, and $p < 0.001$) (Figure 6.2B). Adjacent affected pixel from calcification was quantitatively analyzed using the distance of the brightened region excluding the actual calcified region determined by FWTM considering various parameters of each DECT vendor (see Materials and Methods).

7.4. Analysis of Adjacent Affected Pixel from Calcification Using Polychromatic Images

First, adjacent affected pixel from calcification was calculated using different kVp levels of polychromatic images. Using

polychromatic images, adjacent affected pixel was compared for each kVp level (Figure 7.2), and the results failed to show significant difference of adjacent affected pixel among kVp levels in both small and large FOV images for each CT vendor (FOV 300 mm, p = 0.167, 0.494 and 0.861 for vendor 1, 2, and 3; FOV 150 mm, p = 0.150, 0.161, and 0.075 for vendor 1, 2, and 3).

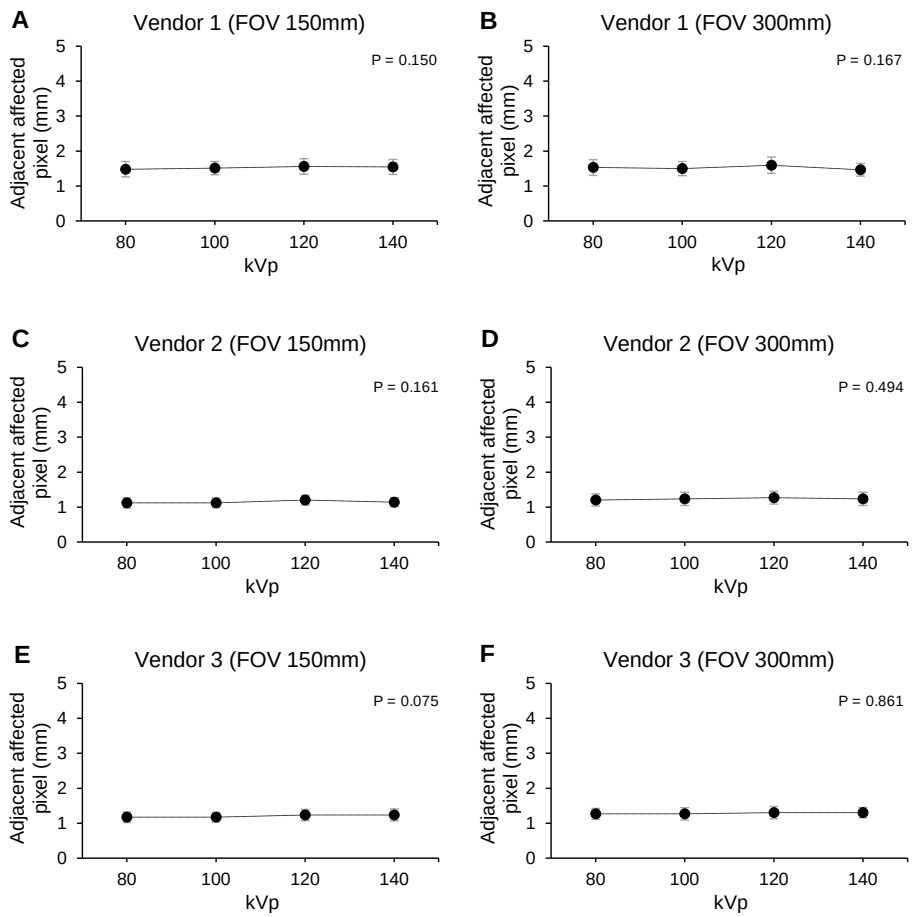

Figure 7.2. Graph plots of adjacent affected pixel from calcification

using different kilovoltage peak levels of polychromatic images. Graph plots of adjacent affected pixel from calcification for different kilovoltage peak levels for small (A, C, and E) or large (B, D, and F) field of view of polychromatic images using vendor 1 (A and B), 2 (C and D), or 3 (E and F). FOV = field of view; kVp = kilovoltage peak; Vendor 1 = Siemens; Vendor 2 = Philips; Vendor 3 = GE; Data are represented as mean ± S.E.M of results. Friedman test was used for the calculation of p−value.

For supplementary results, adjacent affected pixel from calcification was calculated using different FOVs of polychromatic images (Supplementary Figure S9A, C, and E). Small FOV failed to show the reduction of adjacent affected pixel when compared with large FOV of polychromatic images. Moreover, adjacent affected pixel from calcification was calculated using different vendors of polychromatic images (Supplementary Figure S10A and B). Vendor 1 showed significant difference with the highest adjacent affected pixel when compared with other vendors for FOV 150 mm, but not for 300 mm. There was no significant difference of adjacent affected pixel between vendor 2 and 3 for polychromatic images. The objective analysis using polychromatic images indicated that

the low kVp level with less radiation dose showed the similar quantitative measurement of adjacent affected pixel from calcification when compared with high kVp level.

7.5. Analysis of Adjacent Affected Pixel from Calcification Using Virtual Monochromatic Images

Next, adjacent affected pixel from calcification was calculated using the different keV levels of virtual monochromatic images. Using virtual monochromatic images, adjacent affected pixel was compared for each keV level, and the results showed different aspects of adjacent affected pixel among different keV levels for each CT vendor (Figure 7.3).

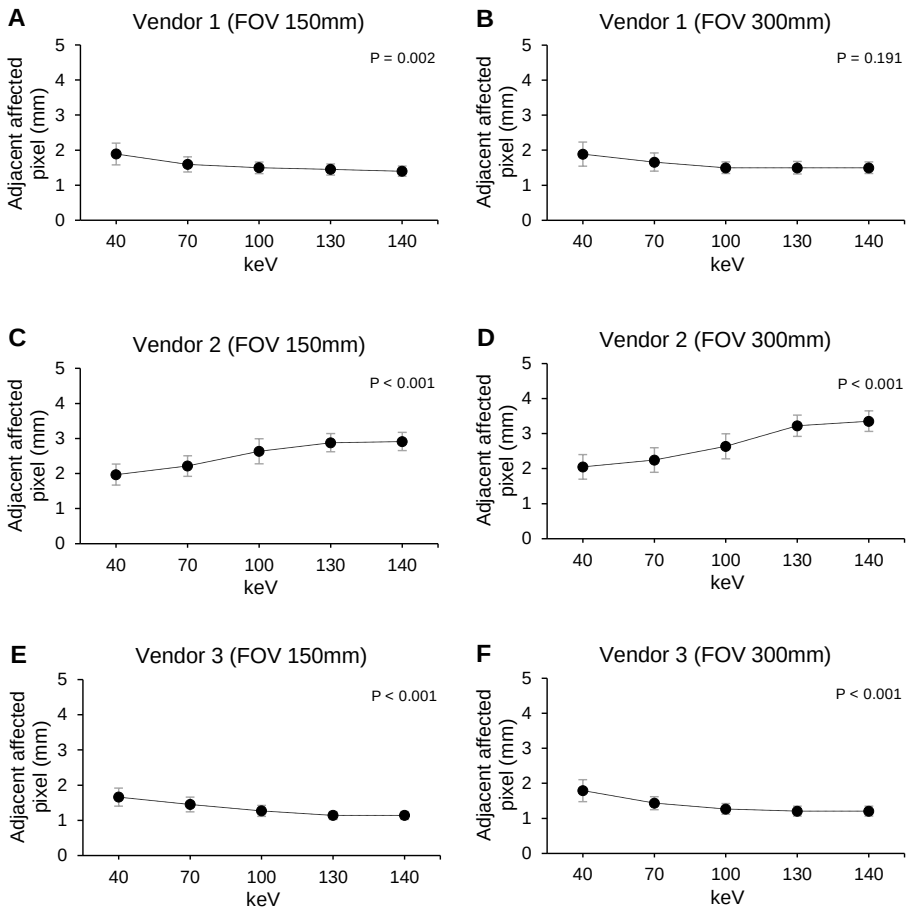

Figure 7.3. Graph plots of adjacent affected pixel from calcification using different kilo-electron volts levels of virtual monochromatic images. Graph plots of adjacent affected pixel from calcification for different kilo-electron volts levels for small (A, C, and E) or large (B, D, and F) field of view of virtual monochromatic images using vendor 1 (A and B), 2 (C and D), or 3 (E and F). FOV = field of view; keV = kilo-electron volts; Vendor 1 = Siemens; Vendor 2 = Philips; Vendor 3 = GE; Data are represented as mean ± S.E.M of

results. Friedman test was used for the calculation of p-value.

For vendor 1, different keV levels did not show significant difference of adjacent affected pixel in large FOV ($p = 0.191$). Adjacent affected pixel increased and decreased with significant difference according to higher keV levels for vendor 2 and 3, respectively ($p < 0.001$). Different aspects of objective quantitative measurement according to keV levels for each CT vendor implied no significant relationship between adjacent affected pixel from calcification and higher X-ray energy level.

Additional analysis was performed to overcome the limitation of higher X-ray energy levels in reducing adjacent affected pixel from calcification with objective quantitative measurement. Adjacent affected pixel from calcification in virtual monochromatic images was compared with that in polychromatic images because existing studies suggested DECT other than conventional CT for reducing blooming artifact by differentiating between iodine and calcium (62-64) (Figure 7.4).

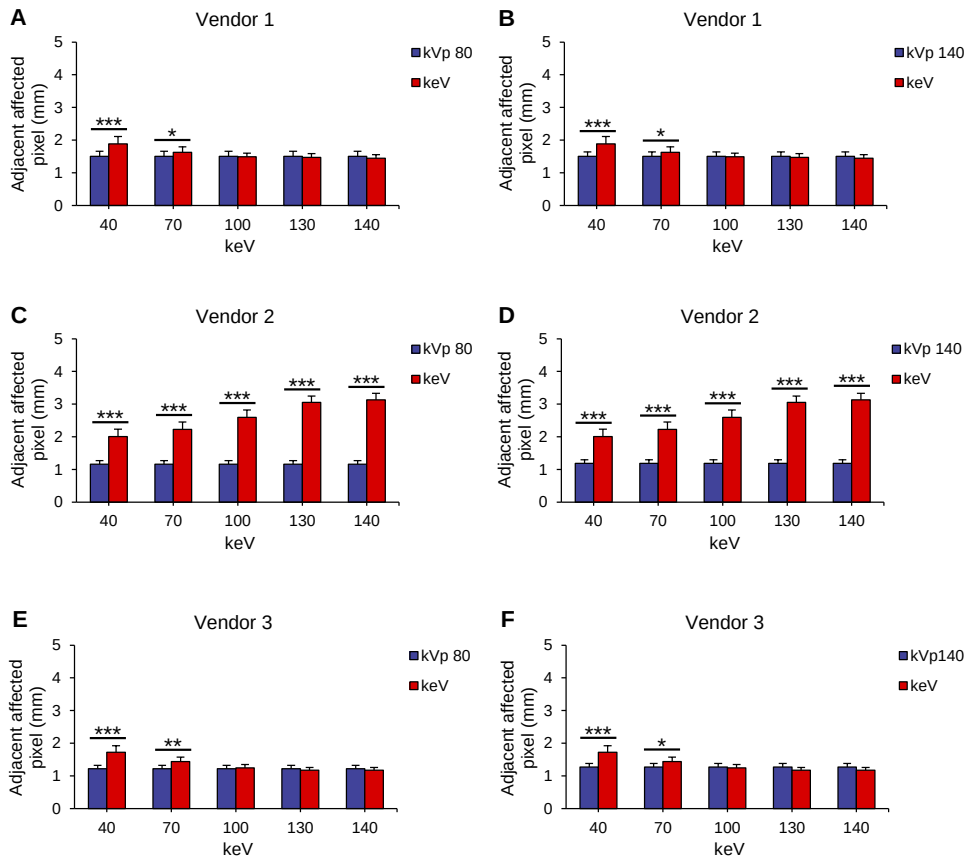

Figure 7.4. Graph plots of adjacent affected pixel from calcification using different images for polychromatic and virtual monochromatic reconstruction. Graph plots of adjacent affected pixel from calcification for different images for polychromatic at kilovoltage peak level of 80 (A, C, and E) or 140 (B, D, and F) with virtual monochromatic reconstruction using vendor 1 (A and B), 2 (C and D), or 3 (E and F). keV = kilo-electron volts; kVp = kilovoltage peak; Vendor 1 = SOMATOM Force, Siemens; Vendor 2 = IQon - Spectral CT, Philips; Vendor 3 = Revolution Apex, GE; Data are

represented as mean + S.E.M of results. *, p−value < 0.05; **, p−value < 0.01; ***, p−value < 0.001; Wilcoxon signed−rank test was used for the calculation of p−value.

Vendor 1 and 3 showed similar aspects of adjacent affected pixel when compared virtual monochromatic with polychromatic images, which was totally different from that of vendor 2. Vendor 1 and 3 showed significant difference with higher adjacent affected pixel in low keV levels of virtual monochromatic images when compared with both low and high kVp levels of polychromatic images (keV 40, $p < 0.001$; kev 70, $p = 0.015$ and 0.004 for vendor 1 and 2) (Figure 7.4A, B, E, and F). However, adjacent affected pixel decreased along higher keV levels in virtual monochromatic images without significant reduction of adjacent affected pixel when compared with polychromatic images in overall. Vendor 2 showed significant difference with higher adjacent affected pixel in virtual monochromatic images when compared to both low and high kVp levels of polychromatic images ($p < 0.001$) (Figure 7.4C and D).

For supplementary results, adjacent affected pixel from calcification was calculated using different FOVs of virtual monochromatic images (Supplementary Figure S9B, D, and F).

Small FOV failed to show the reduction of adjacent affected pixel except for the high keV levels in virtual monochromatic images of vendor 2 (130 or 140 keV). Moreover, adjacent affected pixel from calcification was calculated using different vendors of virtual monochromatic images (Supplementary Figure S10C and D). For high keV levels, vendor 2 showed significant difference in adjacent affected pixel when compared with vendor 1 and 3 for both small and large FOV images because adjacent affected pixel increased along the higher keV levels for vendor 2 (Supplementary Figure S10C and D). The objective quantitative measurement showed that higher keV levels in each vendor influenced differently without significant reduction of adjacent affected pixel from calcification.

7.6. Analysis of Adjacent Affected Pixel from Calcification Using Geometry Difference

In the clinical field, the size or shape difference such as heavily dense calcification may disturb the accuracy of evaluating stenosis degree of lumen. Therefore, supplement to the analysis of adjacent affected pixel from calcification using the X-ray energy difference of polychromatic and virtual monochromatic images, adjacent affected pixel was additionally analyzed using the different

geometries of calcification such as size, shape, or degree. First, adjacent affected pixel was compared with different sizes of calcification using concentric shape with diameter of 4, 5, and 6 mm (Supplementary Figure S11). The result failed to show significant difference of adjacent affected pixel among the sizes of calcification in both small and large FOV images for each CT vendor (FOV 300 mm, p = 0.717 and 0.368 for vendor 1 and 3; FOV 150 mm, p = 0.553 for vendor 2). Second, adjacent affected pixel was compared with concentric and eccentric shapes of calcification (Supplementary Figure S12). 13 out of 18 different shapes did not show significant difference of adjacent affected pixel in both small and large FOV images for each CT vendor. Finally, adjacent affected pixel was compared with different degrees (mild, moderate, and severe) of calcification using the tube shape (Supplementary Figure S13). The result failed to show significant difference of adjacent affected pixel among the degrees of calcification in both small and large FOV images for each CT vendor (FOV 300 mm, p = 0.303 and 0.066 for vendor 1 and 3; FOV 150 mm, p = 0.542 and 0.063 for vendor 1 and 2). This result showed no relationship between adjacent affected pixel from calcification and geometry difference.

Chapter 8. Conclusion and Future Works

CAD is the cause of public health problems worldwide inducing various problems related to the cardiovascular systems (1, 3, 4). CT is a well-known imaging modality which enables non-invasive evaluation of CAD (5-8). However, CT images for patient with dense coronary calcification exhibit blooming artifact when compared to coronary angiography images (50-53). This circumstance may induce the underestimation of coronary lumen diameter or area when evaluating CAD (50-53). Previous studies suggested that increasing kVp in conventional polychromatic images or virtual monochromatic images with higher keV level can reduce blooming artifact from calcification (54-57). However, we hypothesized that higher X-ray energy levels may decrease blooming artifact from calcification with subjective visual assessment in CT images, but fail to reduce adjacent affected pixel from calcification with objective quantitative measurement. Therefore, this research has focused on the quantitative analysis of adjacent affected pixel from calcification using different X-ray energy levels such as kVp or keV through a phantom study. To this end, a phantom was manufactured to acquire polychromatic and

virtual monochromatic images considering various X-ray energy levels using different DECT scanners. Adjacent affected pixel from calcification was quantitatively calculated by subtracting the brightened region from the actual calcified region determined by FWTM. Analysis of adjacent affected pixel from calcification led to the following conclusions: (i) the higher kVp levels in polychromatic images did not reduce adjacent affected pixel from calcification (FOV 300 mm, p = 0.167, 0.494, and 0.861; FOV 150 mm, p = 0.150, 0.161, and 0.075 for vendor 1, 2, and 3). (ii) The higher keV levels failed to significantly reduce objective quantitative measurement of adjacent affected pixel from calcification for virtual monochromatic images reconstructed with three dual energy implementation methods (FOV 300 mm, no significant difference [p = 0.191], increase [p < 0.001], and decrease [p <0.001] for vendor 1, 2, and 3).

Blooming artifact from calcification appearing in CT images is an important issue in coronary artery lumen segmentation (65). For accurate lumen segmentation, the exact separation between lumen and calcium regions is a critical factor. However, blooming artifact from calcification mainly induces the false detection of lumen boundaries (65). Previous studies showed the reduction of blooming

artifact from calcification in higher X-ray energy levels with subjective visual assessment, but not with objective quantitative measurement (54-57). This study firstly quantitatively measured adjacent affected pixel from calcification with a novel method which used FWTM as the actual calcified region. As a result, objective quantitative measurement of adjacent affected pixel from calcification showed no relationship with higher X-ray energy levels which can be applied to the improvement and development of software platforms segmenting coronary artery lumen using CT images.

Moreover, adjacent affected pixel from calcification was quantitatively measured for each CT vendor because there is currently no study which compared brightened region from calcification using different commercial CT scanners. Due to the different parameters among CT vendors such as volume computed tomography dose index (CTDIvol), collimation, rotation time, pitch, and mA, there was a limitation in the accurate comparison (Supplementary Table S3 and S4, see Materials and Methods). Nevertheless, the results showed decreasing adjacent affected pixel with higher keV levels in vendor 1 and 3. Virtual monochromatic images from vendor 2 showed the highest CNR and SNR with the

lowest noise. However, the virtual monochromatic images from vendor 2 showed significant difference when compared with other vendors with increasing adjacent affected pixel at higher keV levels. The difference in kVp levels using polychromatic images showed no significant difference in reducing adjacent affected pixel for all vendors. However, the result of using different keV levels in virtual monochromatic images showed different aspects for each vendor which implied that the different approaches are necessary for reducing adjacent affected pixel from calcification in each vendor for the current circumstances. In the future, high keV levels in virtual monochromatic images would be a critical solution for reducing adjacent affected pixel from calcification with the improvement of CT scanners.

This study has limitations of using a phantom instead of human CT images. However, the phantom has an advantage in quantitative measurement of adjacent affected pixel from calcification because the information of actual diameter or area from calcification is provided. In addition to the results of this study, some future works with a phantom can be performed which better represents the calcification of the actual coronary artery. First, this study used a phantom containing only calcium, but a phantom manufactured

with calcium and a contrast agent will provide more qualitative information for analyzing adjacent affected pixel from calcification. Second, this study focused on adjacent affected pixel from calcification based on X-ray energy difference, but analysis of concentration difference of calcification might provide new insights about blooming effect. Finally, the CT images of human have information of motion because of the constant heart beating. This study used fixed CT images of the phantom which contained no motion information. The analysis of a phantom containing calcium with motion information will better assist in understanding blooming effect.

In summary, adjacent affected pixel from calcification was quantitatively measured using the distance of the brightened region excluding the actual calcified region determined by FWTM. The result showed that the change in X-ray energy levels such as kVp or keV in polychromatic or virtual monochromatic images did not show the reduction of adjacent affected pixel from calcification. This study indicates that higher X-ray energy levels such as kVp or keV decrease blooming artifact from calcification with subjective visual assessment, but fail to reduce adjacent affected pixel from calcification with objective quantitative measurement.

Supplementary Material

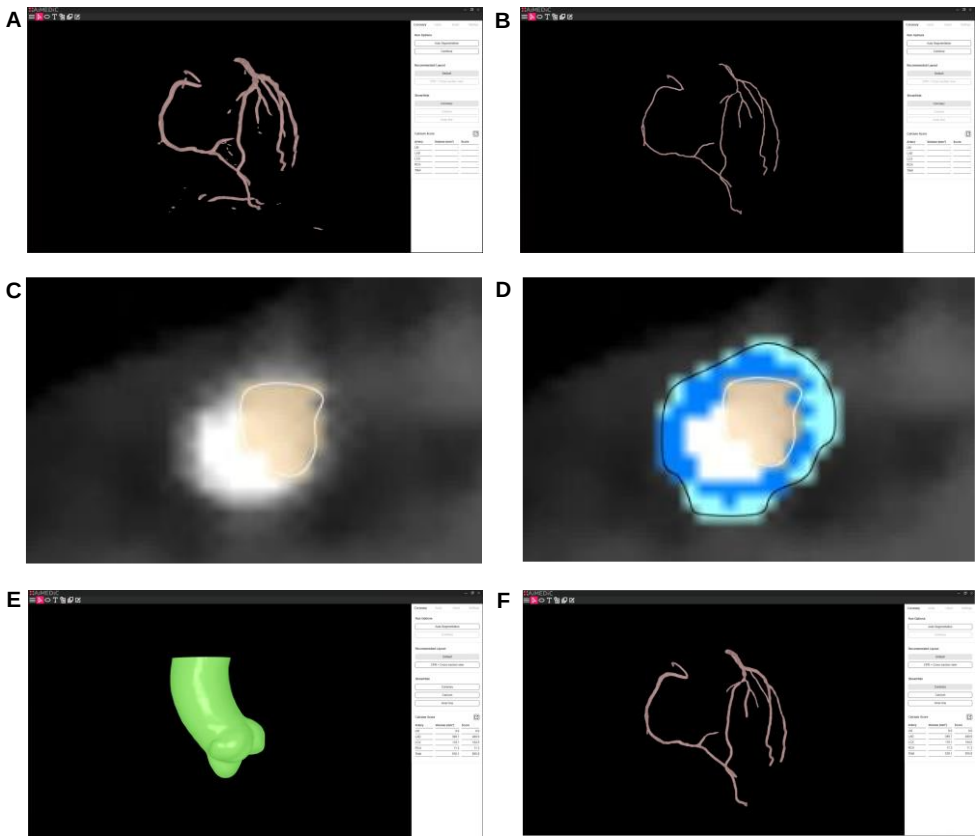

Supplementary Figure S1. New location-adaptive threshold method for calculating lumen or plaque area.

(A) A three-dimensional model of coronary arteries generated by artificial intelligence techniques. (B) The skeleton of coronary arteries considering the removal of calcified plaques and veins. (C-D) The cross-sectional planes of coronary lumen (C) or vessel (D) boundaries. (E) A three-dimensional model of an ascending aorta generated by an automatic segmentation using a deep learning

model. (F) The final three-dimensional model of coronary arteries generated by the new location-adaptive threshold method.

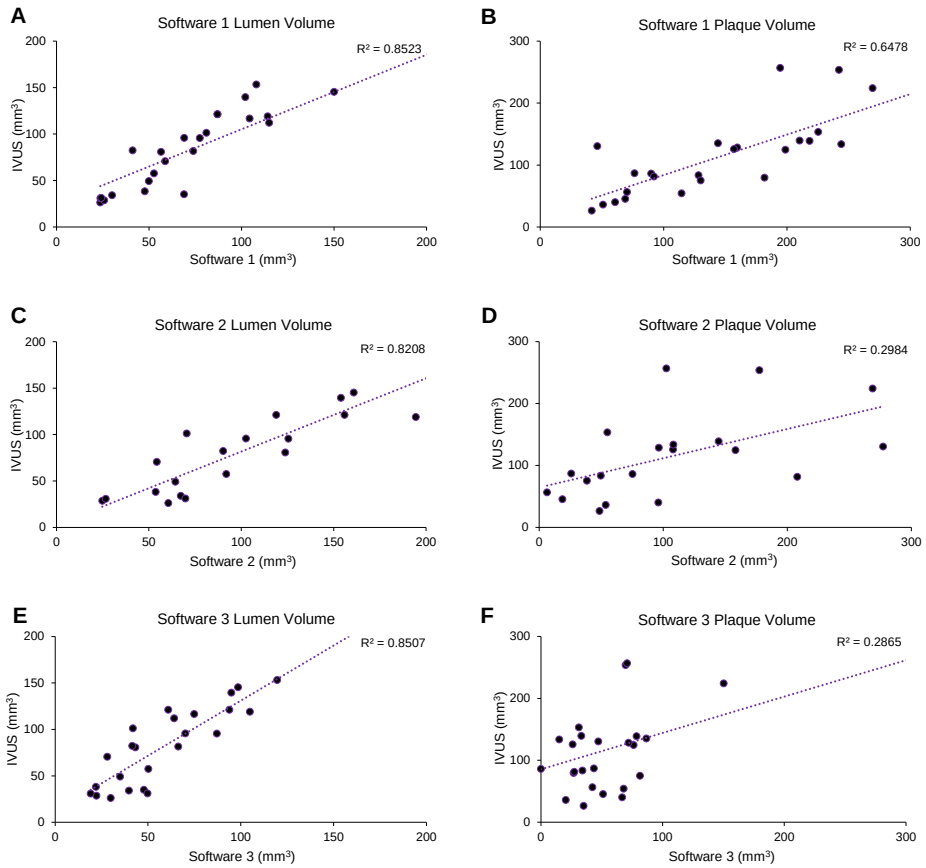

Supplementary Figure S2. Pearson correlation coefficient plots of lumen or plaque volume of each software platform based on IVUS data sets.

Pearson correlation coefficient plots of lumen (A, C, and E) or plaque volume (B, D, and E) of software 1 (A and B), 2 (C and D), or 3 (E and F) based on IVUS data. R^2 = coefficient of

determination; Software 1 = AutoSeg, AiMedic; Software 2 = Syngo.via, Siemens; Software 3 = IntelliSpace Portal, Philips

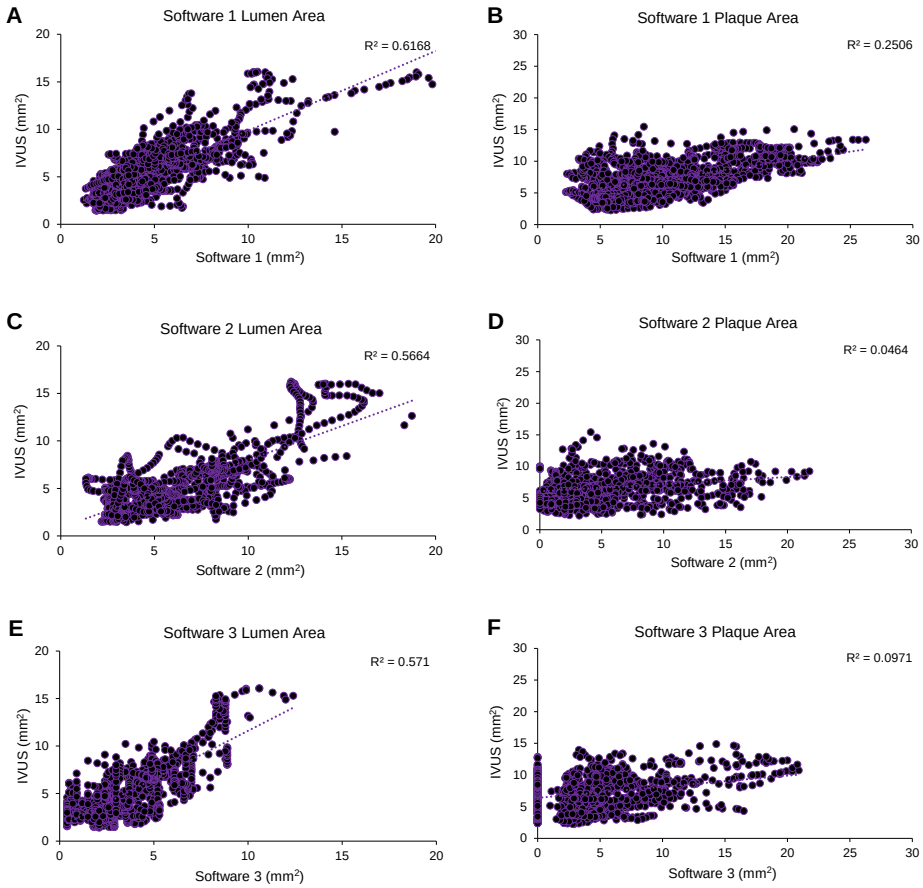

Supplementary Figure S3. Pearson correlation coefficient plots of lumen or plaque area of each software platform based on IVUS data sets.

Pearson correlation coefficient plots of lumen (A, C, and E) or plaque area (B, D, and E) of software 1 (A and B), 2 (C and D), or 3 (E and F) based on IVUS data. R^2 = coefficient of determination;

Software 1 = AutoSeg, AiMedic; Software 2 = Syngo.via, Siemens; Software 3 = IntelliSpace Portal, Philips

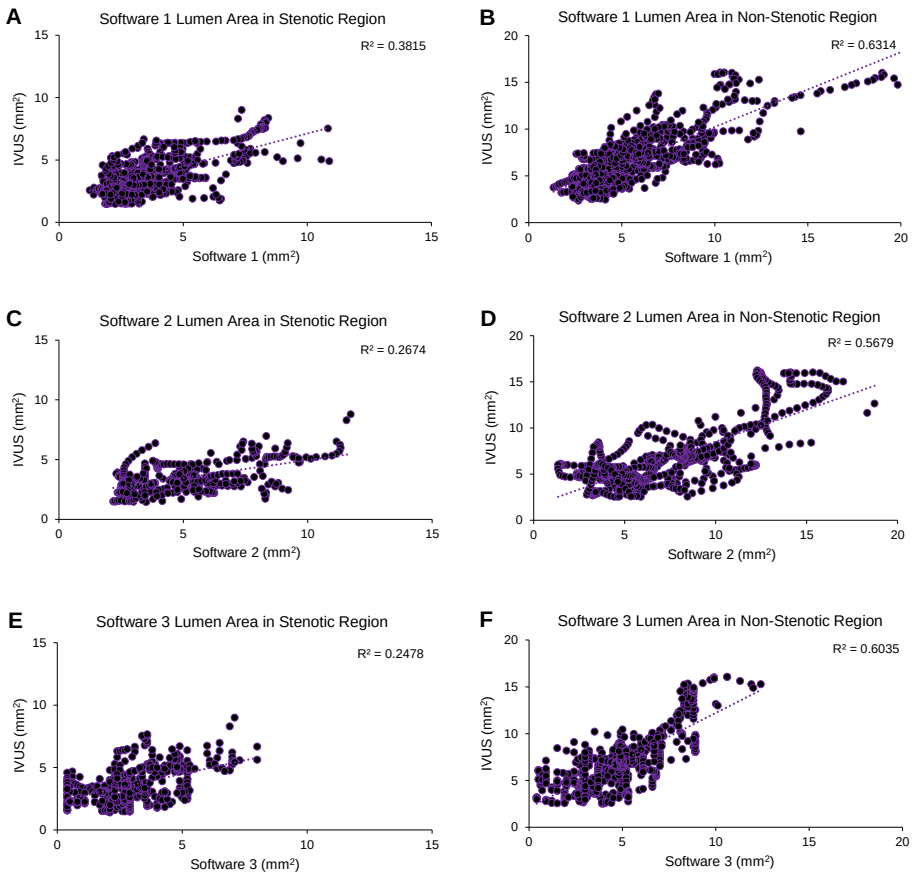

Supplementary Figure S4. Pearson correlation coefficient plots of lumen area in stenotic or non-stenotic region of each software platform based on IVUS data sets.

Pearson correlation coefficient plots of lumen area in stenotic (A, C, and E) or non-stenotic region (B, D, and F) of software 1 (A and B), 2 (C and D), or 3 (E and F) based on IVUS data. R^2 =

coefficient of determination; Software 1 = AutoSeg, AiMedic; Software 2 = Syngo.via, Siemens; Software 3 = IntelliSpace Portal, Philips

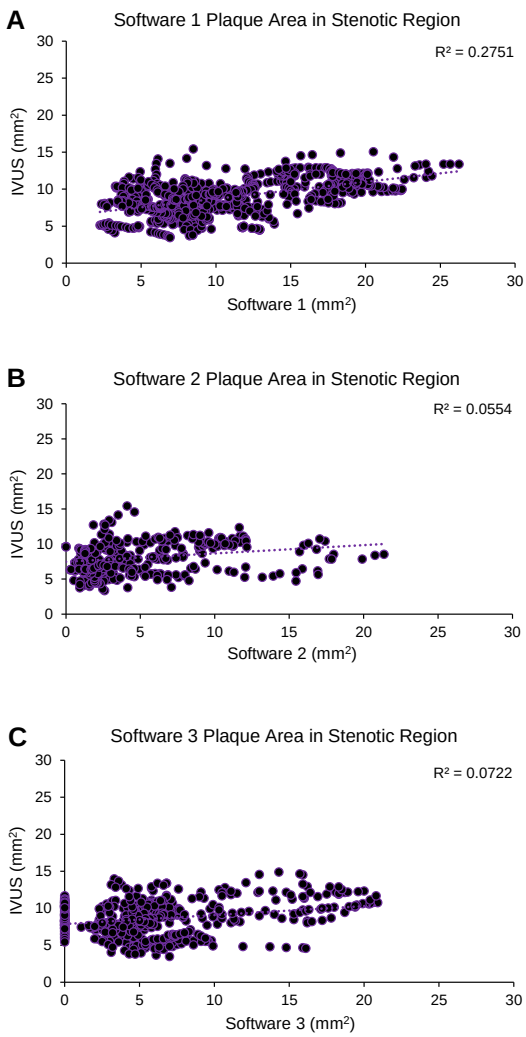

Supplementary Figure S5. Pearson correlation coefficient plots of plaque area in stenotic region of each software platform based on IVUS data sets.

Pearson correlation coefficient plots of plaque area in stenotic region of software 1 (A), 2 (B), or 3 (C) based on IVUS data. R^2 = coefficient of determination; Software 1 = AutoSeg, AiMedic; Software 2 = Syngo.via, Siemens; Software 3 = IntelliSpace Portal, Philips

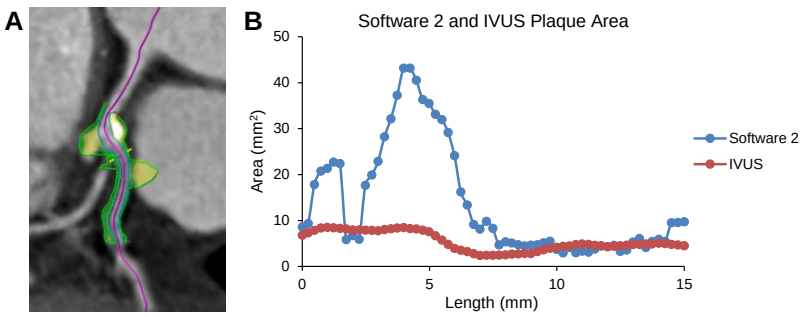

Supplementary Figure S6. Exclusion criteria for plaque area.

A curved planar reformation image (A) and plaque area graph of software 2 and IVUS (B) using a representative case.

Software 2 = Syngo.via, Siemens

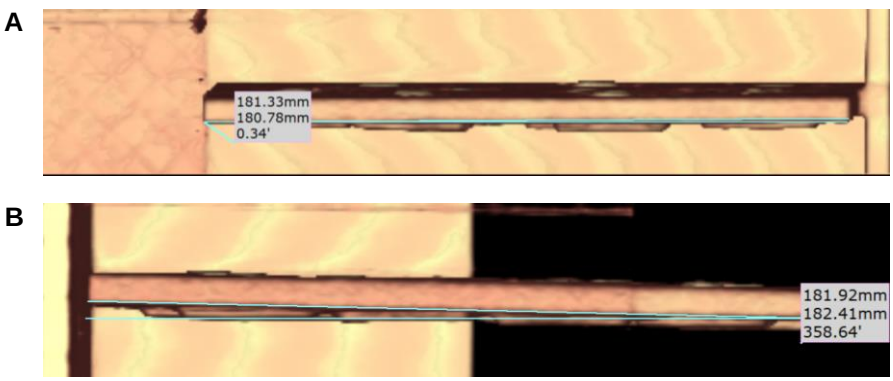

Supplementary Figure S7. Measurement of distortion angles of a phantom.

Distortion angle in (A) anterior or (B) left view of a phantom. Three-dimensional images of a phantom were used for measuring the distortion angle in degrees.

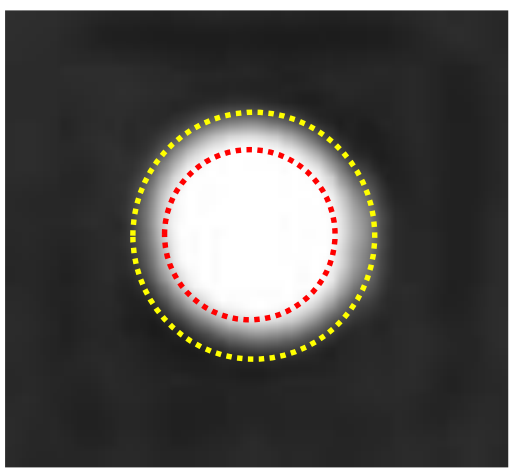

Supplementary Figure S8. A computed tomography image of calcification with indicated boundaries.

Red and yellow dotted lines indicate the boundaries of the actual calcified region determined by full width at third maximum and brightened region calculated by 5% to the maximum brightness of calcification, respectively.

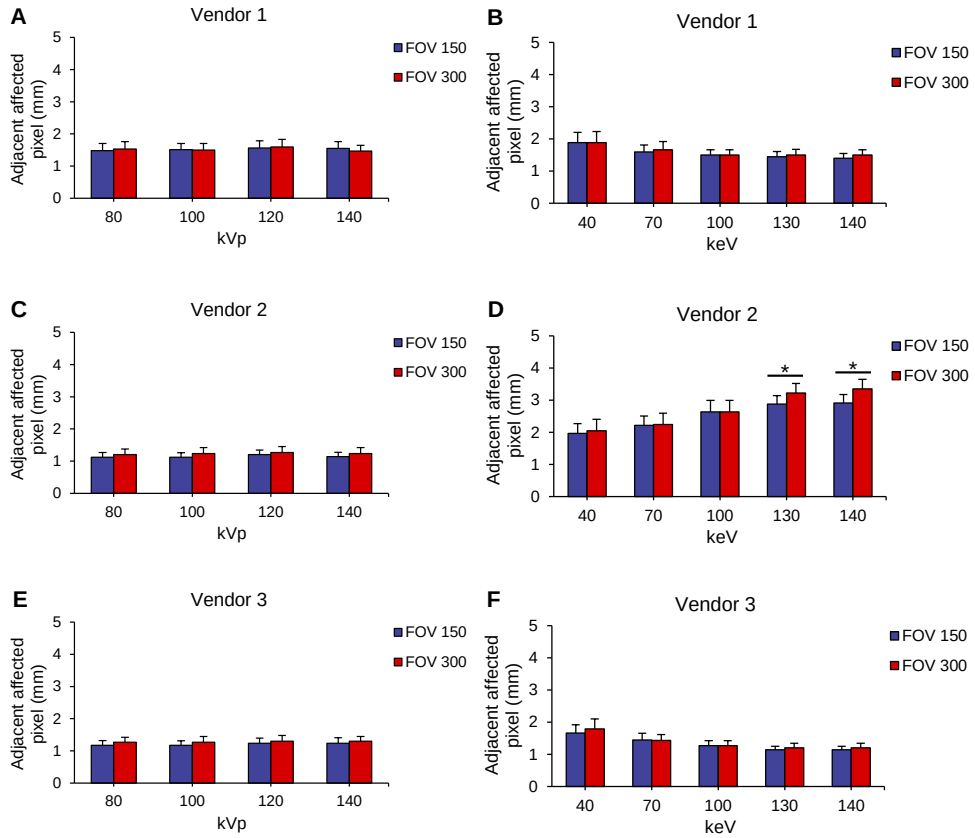

Supplementary Figure S9. Graph plots of adjacent affected pixel from calcification using different field of views.

Graph plots of adjacent affected pixel from calcification for different field of views for polychromatic (A, C, and E) or virtual monochromatic (B, D, and F) images using vendor 1 (A and B), 2 (C and D), or 3 (E and F). FOV = field of view; keV = kilo-electron volts; kVp = kilovoltage peak; Vendor 1 = Siemens; Vendor 2 = Philips; Vendor 3 = GE; Data are represented as mean + S.E.M of results. *, p-value < 0.05; Wilcoxon signed-rank test was used for

the calculation of p-value.

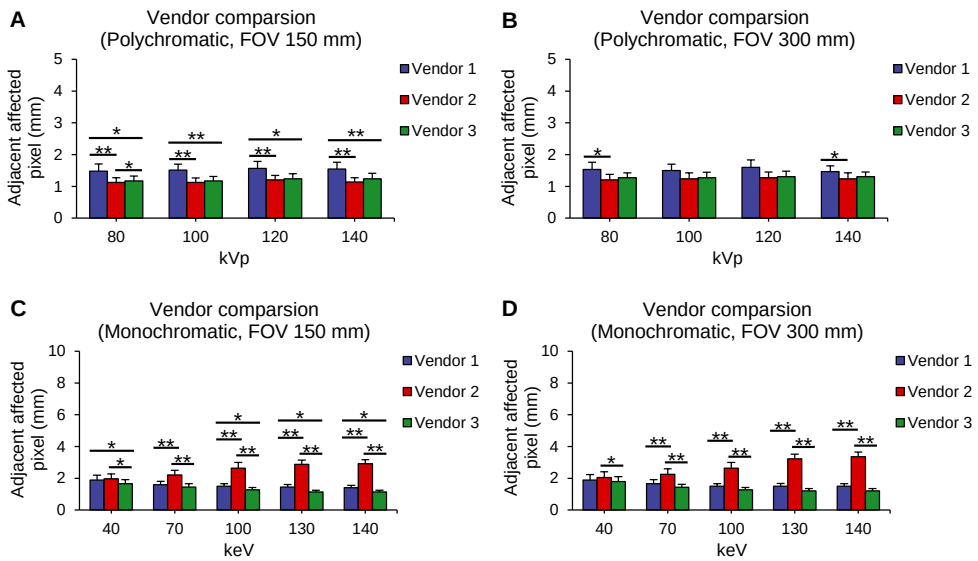

Supplementary Figure S10. Graph plots of adjacent affected pixel from calcification of different vendors using various parameters.

Graph plots of adjacent affected pixel from calcification for different vendors using small (A and C) or large (B and D) field of views for polychromatic (A and B) or virtual monochromatic (C and D) images. FOV = field of view; keV = kilo-electron volts; kVp = kilovoltage peak; Vendor 1 = Siemens; Vendor 2 = Philips; Vendor 3 = GE; Data are represented as mean + S.E.M of results. *, p-value < 0.05; **, p-value < 0.01; Wilcoxon signed-rank test was used for the calculation of p-value.

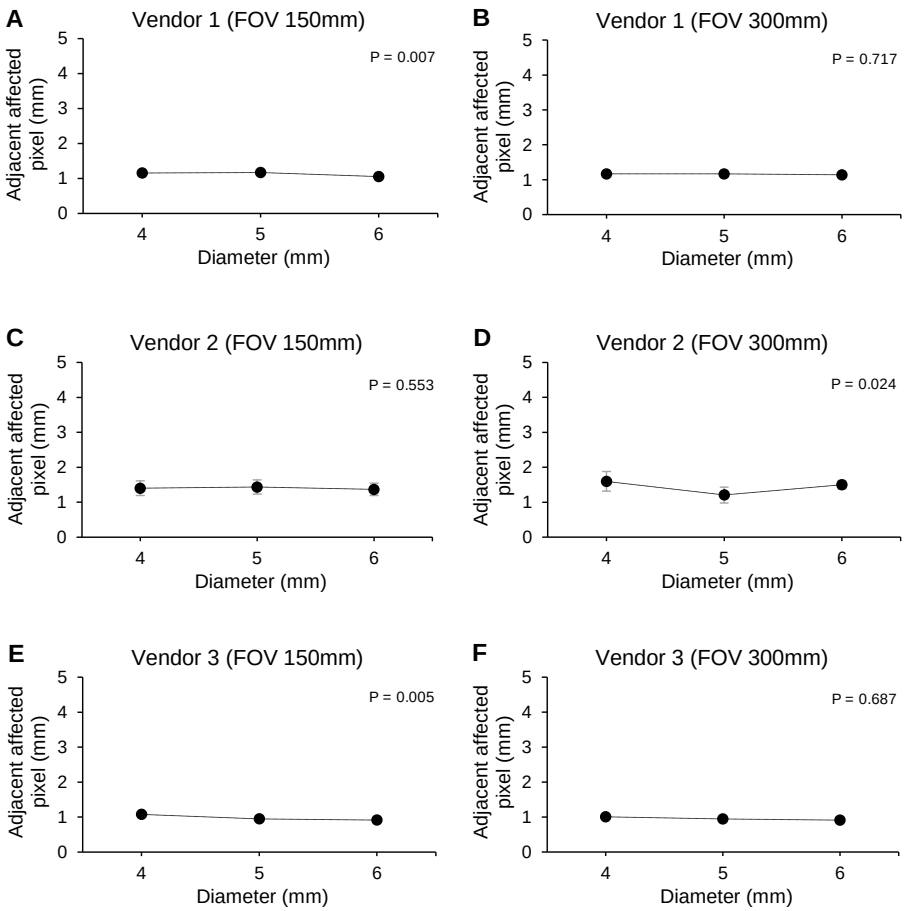

Supplementary Figure S11. Graph plots of adjacent affected pixel from calcification using different sizes of the concentric shape.

Graph plots of adjacent affected pixel from calcification for different sizes of the concentric shape for small (A, C, and E) or large (B, D, and F) field of view using vendor 1 (A and B), 2 (C and D), or 3 (E and F). FOV = field of view; Vendor 1 = Siemens; Vendor 2 = Philips; Vendor 3 = GE; Data are represented as mean ± S.E.M of results. Friedman test was used for the calculation of p-value.

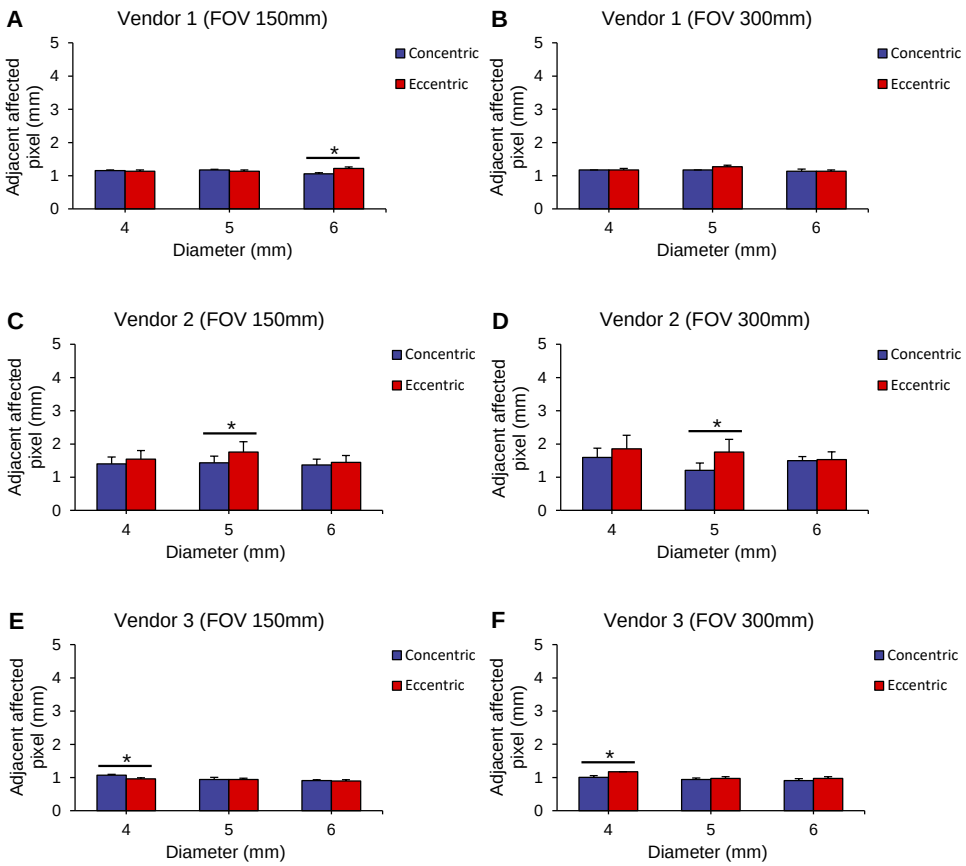

Supplementary Figure S12. Graph plots of adjacent affected pixel comparing concentric and eccentric shapes of calcification using different sizes.

Graph plots of adjacent affected pixel comparing concentric and eccentric shapes of calcification for small (A, C, and E) or large (B, D, and F) field of view using vendor 1 (A and B), 2 (C and D), or 3 (E and F). FOV = field of view; Vendor 1 = Siemens; Vendor 2 = Philips; Vendor 3 = GE; Data are represented as mean + S.E.M of

results. *, p-value < 0.05; Wilcoxon signed-rank test was used for the calculation of p-value.

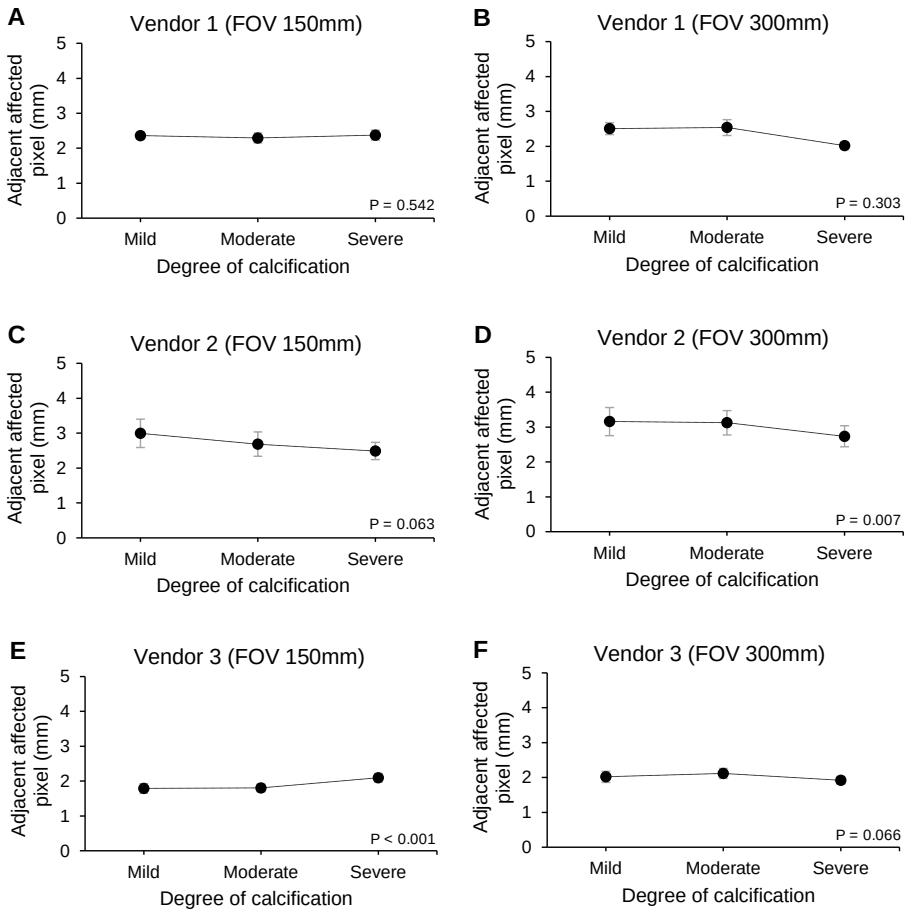

Supplementary Figure S13. Graph plots of adjacent affected pixel comparing mild, moderate, and severe degrees of calcification using the tube shape.

Graph plots of adjacent affected pixel comparing mild, moderate, and severe degrees of calcification using the tube shape for small

(A, C, and E) or large (B, D, and F) field of view using vendor 1 (A and B), 2 (C and D), or 3 (E and F). FOV = field of view; Vendor 1 = Siemens; Vendor 2 = Philips; Vendor 3 = GE; Data are represented as mean ± S.E.M of results. Friedman test was used for the calculation of p-value.

Supplementary Table S1. Failure rate of each condition for different software platforms.

	Failure rate (%)		
	Software 1	Software 2	Software 3
DICOM file open	0.0	21.5	0.0
Lumen volume	3.8	0.0	3.8
Plaque volume	3.8	4.8	0.0
Lumen area	1.6	0.7	1.2
Plaque area	1.6	7.0	0.8

DICOM = Digital Imaging and Communications in Medicine; Software 1 = AutoSeg, AiMedic; Software 2 = Syngo.via, Siemens; Software 3 = IntelliSpace Portal, Philip

Supplementary Table S2. Number of cross-sectional planes of coronary segments for different software platforms.

	Number of cross-sectional planes		
	Software 1	Software 2	Software 3
Lumen area	1795	1100	1313
Plaque area	1795	1029	1319
Lumen area in stenotic region	725	390	516
Lumen area in non-stenotic region	1070	710	797
Plaque area in stenotic region	730	332	514

Software 1 = AutoSeg, AiMedic; Software 2 = Syngo.via, Siemens; Software 3 = IntelliSpace Portal, Philip

Supplementary Table S3. Computed tomography parameters for different vendors.

	Polychromatic image			Virtual monochromatic image		
	Vendor 1	Vendor 2	Vendor 3	Vendor 1	Vendor 2	Vendor 3
kVp	80, 100, 120, 140	80, 100, 120, 140	80, 100, 120, 140	80 / 140 (dual source)	140 (single source)	80 / 140 (fast switching)
keV	NA	NA	NA	40, 70, 100 ,130, 140	40, 70, 100 ,130, 140	40, 70, 100 ,130, 140
Field of view (mm)	150, 300	150, 300	150, 300	150, 300	150, 300	150, 300
Tube current (mA)	250	250	250	240 / 120	250	250
Scan type	Helical (Abdomen)	Helical (Abdomen)	Helical (Abdomen)	Helical (Abdomen)	Helical (Abdomen)	Helical (Abdomen)
Rotation time (sec)	0.5	0.33	1	0.5	0.33	1
Collimation (mm)	192 * 0.6	16 * 0.625	40 * 0.625	128 * 0.6	16 * 0.625	40 * 0.625
Pitch	0.6: 1	0.799: 1	0.984: 1	0.6: 1	0.799: 1	0.984: 1
Slice thickness (mm)	0.6	0.8	0.625	0.6	0.8	0.625
Reconstruction algorithm	Br40	IMR1	Standard	Qr40	Spectral	Standard

keV = kilo-electron volts; kVp = kilovoltage peak; NA = not applicable; Vendor 1 = Siemens; Vendor 2 = Philips; Vendor 3 = GE

Supplementary Table S4. Volume computed tomography dose index for different vendors.

	CTDIvol (mGy)		
	Vendor 1	Vendor 2	Vendor 3
kVp 80	4.79	8.50	3.31
kVp 100	10.01	16.30	6.49
kVp 120	16.69	25.70	10.48
kVp 140	24.34	37.00	15.26
keV	17.16	37.00	8.34

CTDIvol = volume computed tomography does index; keV = kilo-electron volts; kVp = kilovolatge peak; Vendor 1 = Siemens; Vendor 2 = Philips; Vendor 3 = GE

Bibliography

1. Amini M, Zayeri F, Salehi M. Trend analysis of cardiovascular disease mortality, incidence, and mortality-to-incidence ratio: Results from global burden of disease study 2017. BMC Public Health 2021;21:401
2. Howson JMM, Zhao W, Barnes DR, Ho WK, Young R, Paul DS et al. Fifteen new risk loci for coronary artery disease highlight arterial-wall-specific mechanisms. Nat Genet 2017;49:1113-1119
3. Musunuru K, Kathiresan S. Genetics of common, complex coronary artery disease. Cell 2019;177:132-145
4. Taylor AJ, Papapostolou S. Finding the right pathway for the assessment of stable coronary artery disease. JACC Cardiovasc Imaging 2022;15:626-628
5. Leschka S, Alkadhi H, Plass A, Desbiolles L, Grunenfelder J, Marincek B et al. Accuracy of msct coronary angiography with 64-slice technology: First experience. Eur Heart J 2005;26:1482-1487
6. Hoffmann MH, Shi H, Schmitz BL, Schmid FT, Lieberknecht M, Schulze R et al. Noninvasive coronary angiography with multislice computed tomography. JAMA 2005;293:2471-

2478

7. de Feyter PJ, Nieman K. Ccta to guide revascularization for high-risk cad: A 'cliff hanger'. Eur Heart J 2012;33:3011-3013

8. Elnabawi YA, Dey AK, Mehta NN. Emerging applications of coronary ct angiography in coronary heart disease: Getting better with time. Eur Heart J 2018;39:3682-3684

9. Boogers MJ, Broersen A, van Velzen JE, de Graaf FR, El-Naggar HM, Kitslaar PH et al. Automated quantification of coronary plaque with computed tomography: Comparison with intravascular ultrasound using a dedicated registration algorithm for fusion-based quantification. Eur Heart J 2012;33:1007-1016

10. Dey D, Schepis T, Marwan M, Slomka PJ, Berman DS, Achenbach S. Automated three-dimensional quantification of noncalcified coronary plaque from coronary ct angiography: Comparison with intravascular us. Radiology 2010;257:516-522

11. Anders K, Achenbach S, Petit I, Daniel WG, Uder M, Pflederer T. Accuracy of automated software-guided detection of significant coronary artery stenosis by ct

angiography: Comparison with invasive catheterisation. Eur Radiol 2013;23:1218-1225

12. Schaap M, Neefjes L, Metz C, van der Giessen A, Weustink A, Mollet N et al. Coronary lumen segmentation using graph cuts and robust kernel regression. Inf Process Med Imaging 2009;21:528-539

13. Cai K, Yang R, Li L, Ou S, Chen Y, Dou J. A semi-automatic coronary artery segmentation framework using mechanical simulation. J Med Syst 2015;39:129

14. Athanasiou L, Rigas G, Sakellarios AI, Exarchos TP, Siogkas PK, Bourantas CV et al. Three-dimensional reconstruction of coronary arteries and plaque morphology using ct angiography--comparison and registration with ivus. BMC Med Imaging 2016;16:9

15. Di Carli M, Czernin J, Hoh CK, Gerbaudo VH, Brunken RC, Huang SC et al. Relation among stenosis severity, myocardial blood flow, and flow reserve in patients with coronary artery disease. Circulation 1995;91:1944-1951

16. Pijls NH, Sels JW. Functional measurement of coronary stenosis. J Am Coll Cardiol 2012;59:1045-1057

17. Choi EK, Choi SI, Rivera JJ, Nasir K, Chang SA, Chun EJ et al.

Coronary computed tomography angiography as a screening tool for the detection of occult coronary artery disease in asymptomatic individuals. J Am Coll Cardiol 2008;52:357-365

18. Ahmadi A, Argulian E, Leipsic J, Newby DE, Narula J. From subclinical atherosclerosis to plaque progression and acute coronary events: Jacc state-of-the-art review. J Am Coll Cardiol 2019;74:1608-1617

19. Gheorghiade M, Bonow RO. Chronic heart failure in the united states: A manifestation of coronary artery disease. Circulation 1998;97:282-289

20. Lesage D, Angelini ED, Bloch I, Funka-Lea G. A review of 3d vessel lumen segmentation techniques: Models, features and extraction schemes. Med Image Anal 2009;13:819-845

21. Shin CI, Park SJ, Kim JH, Yoon YE, Park EA, Koo BK et al. Coronary artery lumen segmentation using location-adaptive threshold in coronary computed tomographic angiography: A proof-of-concept. Korean J Radiol 2021;22:688-696

22. Abbara S, Arbab-Zadeh A, Callister TQ, Desai MY, Mamuya W, Thomson L et al. Scct guidelines for performance of coronary computed tomographic angiography: A report of the

society of cardiovascular computed tomography guidelines committee. J Cardiovasc Comput Tomogr 2009;3:190-204

23. Milletari F, Navab N, Ahmadi S-A. V-net: Fully convolutional neural networks for volumetric medical image segmentation. In:2016 fourth international conference on 3D vision (3DV): IEEE, 2016; 565-571.

24. Chen L-C, Zhu Y, Papandreou G, Schroff F, Adam H. Encoder-decoder with atrous separable convolution for semantic image segmentation. In:Proceedings of the European conference on computer vision (ECCV), 2018; 801-818.

25. Reynolds DA. Gaussian mixture models. Encyclopedia of biometrics 2009;741

26. Moon TK. The expectation-maximization algorithm. IEEE Signal processing magazine 1996;13:47-60

27. Lefkimmiatis S, Bourquard A, Unser M. Hessian-based norm regularization for image restoration with biomedical applications. IEEE Transactions on Image Processing 2011;21:983-995

28. Chen T, Guestrin C. Xgboost: A scalable tree boosting system. In:Proceedings of the 22nd acm sigkdd international

conference on knowledge discovery and data mining, 2016; 785-794.

29. Bland JM, Altman DG. Measuring agreement in method comparison studies. Stat Methods Med Res 1999;8:135-160

30. Shrout PE, Fleiss JL. Intraclass correlations: Uses in assessing rater reliability. Psychol Bull 1979;86:420-428

31. Benesty J, Chen J, Huang Y, Cohen I. Pearson correlation coefficient. InNoise reduction in speech processing: Springer, 2009:1-4.

32. Diedenhofen B, Musch J. Cocor: A comprehensive solution for the statistical comparison of correlations. PLoS One 2015;10:e0121945

33. Maurovich-Horvat P, Ferencik M, Voros S, Merkely B, Hoffmann U. Comprehensive plaque assessment by coronary ct angiography. Nat Rev Cardiol 2014;11:390-402

34. Luo T, Wischgoll T, Kwon Koo B, Huo Y, Kassab GS. Ivus validation of patient coronary artery lumen area obtained from ct images. PLoS One 2014;9:e86949

35. Xaplanteris P, Fournier S, Pijls NHJ, Fearon WF, Barbato E, Tonino PAL et al. Five-year outcomes with pci guided by fractional flow reserve. N Engl J Med 2018;379:250-259

36. Petraco R, Sen S, Nijjer S, Echavarria-Pinto M, Escaned J, Francis DP et al. Fractional flow reserve-guided revascularization: Practical implications of a diagnostic gray zone and measurement variability on clinical decisions. JACC Cardiovasc Interv 2013;6:222-225

37. Pijls NH, Fearon WF, Tonino PA, Siebert U, Ikeno F, Bornschein B et al. Fractional flow reserve versus angiography for guiding percutaneous coronary intervention in patients with multivessel coronary artery disease: 2-year follow-up of the fame (fractional flow reserve versus angiography for multivessel evaluation) study. J Am Coll Cardiol 2010;56:177-184

38. Morris PD, Ryan D, Morton AC, Lycett R, Lawford PV, Hose DR et al. Virtual fractional flow reserve from coronary angiography: Modeling the significance of coronary lesions: Results from the virtu-1 (virtual fractional flow reserve from coronary angiography) study. JACC Cardiovasc Interv 2013;6:149-157

39. Min JK, Taylor CA, Achenbach S, Koo BK, Leipsic J, Norgaard BL et al. Noninvasive fractional flow reserve derived from coronary ct angiography: Clinical data and

scientific principles. JACC Cardiovasc Imaging 2015;8:1209-1222

40. Koo BK, Erglis A, Doh JH, Daniels DV, Jegere S, Kim HS et al. Diagnosis of ischemia-causing coronary stenoses by noninvasive fractional flow reserve computed from coronary computed tomographic angiograms. Results from the prospective multicenter discover-flow (diagnosis of ischemia-causing stenoses obtained via noninvasive fractional flow reserve) study. J Am Coll Cardiol 2011;58:1989-1997

41. Taylor CA, Fonte TA, Min JK. Computational fluid dynamics applied to cardiac computed tomography for noninvasive quantification of fractional flow reserve: Scientific basis. J Am Coll Cardiol 2013;61:2233-2241

42. Driessen RS, Danad I, Stuijfzand WJ, Raijmakers PG, Schumacher SP, van Diemen PA et al. Comparison of coronary computed tomography angiography, fractional flow reserve, and perfusion imaging for ischemia diagnosis. J Am Coll Cardiol 2019;73:161-173

43. Hlatky MA, De Bruyne B, Pontone G, Patel MR, Norgaard BL, Byrne RA et al. Quality-of-life and economic outcomes of

assessing fractional flow reserve with computed tomography angiography: Platform. J Am Coll Cardiol 2015;66:2315-2323

44. Collet C, Miyazaki Y, Ryan N, Asano T, Tenekecioglu E, Sonck J et al. Fractional flow reserve derived from computed tomographic angiography in patients with multivessel cad. J Am Coll Cardiol 2018;71:2756-2769

45. Agrawal MD, Pinho DF, Kulkarni NM, Hahn PF, Guimaraes AR, Sahani DV. Oncologic applications of dual-energy ct in the abdomen. Radiographics 2014;34:589-612

46. McCollough CH, Leng S, Yu L, Fletcher JG. Dual- and multi-energy ct: Principles, technical approaches, and clinical applications. Radiology 2015;276:637-653

47. Johnson TR. Dual-energy ct: General principles. AJR Am J Roentgenol 2012;199:S3-8

48. Danad I, Fayad ZA, Willemink MJ, Min JK. New applications of cardiac computed tomography: Dual-energy, spectral, and molecular ct imaging. JACC Cardiovasc Imaging 2015;8:710-723

49. Yu L, Leng S, McCollough CH. Dual-energy ct-based monochromatic imaging. AJR Am J Roentgenol

2012;199:S9-S15

50. Kruk M, Noll D, Achenbach S, Mintz GS, Pregowski J, Kaczmarska E et al. Impact of coronary artery calcium characteristics on accuracy of ct angiography. JACC Cardiovasc Imaging 2014;7:49-58

51. Hoffmann U, Moselewski F, Cury RC, Ferencik M, Jang IK, Diaz LJ et al. Predictive value of 16-slice multidetector spiral computed tomography to detect significant obstructive coronary artery disease in patients at high risk for coronary artery disease: Patient-versus segment-based analysis. Circulation 2004;110:2638-2643

52. Brodoefel H, Burgstahler C, Tsiflikas I, Reimann A, Schroeder S, Claussen CD et al. Dual-source ct: Effect of heart rate, heart rate variability, and calcification on image quality and diagnostic accuracy. Radiology 2008;247:346-355

53. Sarwar A, Rieber J, Mooyaart EA, Seneviratne SK, Houser SL, Bamberg F et al. Calcified plaque: Measurement of area at thin-section flat-panel ct and 64-section multidetector ct and comparison with histopathologic findings. Radiology 2008;249:301-306

54. Kalisz K, Buethe J, Saboo SS, Abbara S, Halliburton S, Rajiah P. Artifacts at cardiac ct: Physics and solutions. Radiographics 2016;36:2064-2083

55. Stocker TJ, Leipsic J, Hadamitzky M, Chen MY, Rubinshtein R, Deseive S et al. Application of low tube potentials in ccta: Results from the protection vi study. JACC Cardiovasc Imaging 2020;13:425-434

56. Albrecht MH, De Cecco CN, Schoepf UJ, Spandorfer A, Eid M, De Santis D et al. Dual-energy ct of the heart current and future status. Eur J Radiol 2018;105:110-118

57. Yunaga H, Ohta Y, Kaetsu Y, Kitao S, Watanabe T, Furuse Y et al. Diagnostic performance of calcification-suppressed coronary ct angiography using rapid kilovolt-switching dual-energy ct. Eur Radiol 2017;27:2794-2801

58. Jacobsen MC, Schellingerhout D, Wood CA, Tamm EP, Godoy MC, Sun J et al. Intermanufacturer comparison of dual-energy ct iodine quantification and monochromatic attenuation: A phantom study. Radiology 2018;287:224-234

59. Xu BL, Zhou WL, Zhu TP, Cheng KY, Li YJ, Zhan HJ et al. A full-width half-maximum method to assess retinal vascular structural changes in patients with ischemic heart disease

and microvascular anginga. Sci Rep 2019;9:11019

60. Rey D, Neuhäuser M. Wilcoxon-signed-rank test. InInternational encyclopedia of statistical science: Springer, 2011:1658-1659.

61. Sheldon MR, Fillyaw MJ, Thompson WD. The use and interpretation of the friedman test in the analysis of ordinal-scale data in repeated measures designs. Physiotherapy Research International 1996;1:221-228

62. Ruzsics B, Lee H, Zwerner PL, Gebregziabher M, Costello P, Schoepf UJ. Dual-energy ct of the heart for diagnosing coronary artery stenosis and myocardial ischemia-initial experience. Eur Radiol 2008;18:2414-2424

63. Schwarz F, Nance JW, Jr., Ruzsics B, Bastarrika G, Sterzik A, Schoepf UJ. Quantification of coronary artery calcium on the basis of dual-energy coronary ct angiography. Radiology 2012;264:700-707

64. Liu P, Wang Y, Jin Z-y. Dual-energy evaluation of high calcium score (> 400) coronary artery. InCardiac ct: Springer, 2020:21-26.

65. Ghanem AM, Hamimi AH, Matta JR, Carass A, Elgarf RM, Gharib AM et al. Automatic coronary wall and atherosclerotic

plaque segmentation from 3d coronary ct angiography. Sci Rep 2019;9:47

Conflict of Interest

The author is a graduate student in Department of Clinical Medical Sciences, Seoul National University College of Medicine as well as an employee of AI Medic, Inc.

Abstract in Korean (국문 초록)

전산화 단층촬영 영상을 이용한 관상동맥 분할의 새로운 위치 적응형 한계치 방법 및 칼슘의 블루밍 아티팩트 분석 연구

파트 1. 전산화 단층촬영 영상을 이용한 관상동맥 분할의 새로운 위치 적응형 한계치 방법 분석 연구

서론

관상동맥 전산화 단층촬영 혈관조영술을 이용하여 관상동맥 자동 분할 기법을 사용하면 관상동맥 질환 관련 다양한 분석을 제공할 수 있다. 다양한 분석을 위해서 관상동맥 내강과 플라크 분할의 정확도를 확보하는 것이 중요하다. 이 연구에서는 새로 개발된 위치 적응형 한계치 방법을 사용하는 소프트웨어의 관상동맥 분할 알고리즘을 현재 상용화되고 있는 소프트웨어들과 비교하고자 하였다.

방법

혈관 내 초음파 영상을 통해 얻은 19명 환자의 26개 타겟 관상동맥 데이터를 표준으로 사용하였다. 소프트웨어들의 분할 알고리즘 성능은 타겟 관상동맥의 내강과 플라크 변수 데이터를 사용하여 분석하였다. 통계 분석은 피어슨 상관계수, 급간 내 상관계수, 블랜드-앨트먼 도표 등을 사용하여 각 소프트웨어와 혈관 내 초음파 영상의 내강과 플라크 변수들에 대한 데이터 비교를 통해 수행하였다.

결과

새로운 위치 적응형 한계치 방법을 사용하는 소프트웨어는 내강 용량과 (평균 차이 = −9.1 mm^3, 95% 신뢰구간 = −18.6에서 0.4 mm^3) 내강 면적 (평균 차이 = −0.72 mm^2, 95% 신뢰구간 = −0.80에서 −0.64 mm^2) 계산에 대한 평균 차이가 가장 작았으며, 피어슨 상관계수와 급간 내 상관계수가 가장 높게 나타났다. 이에 더하여, 내강과 플라크 면적에 대한 소그룹 분석 결과를 보았을 때, 새로운 위치 적응형 한계치 방법을 사용하는 소프트웨어는 협착 지역에서 내강과 (평균 차이 = −0.07 mm^2, 95% 신뢰구간 = −0.16에서 0.02 mm^2) 플라크 면적 (평균 차이 = 1.70 mm^2, 95% 신뢰구간 = 1.37에서 2.03 mm^2) 계산에 대한 평균 차이가 가장 작았으며, 현재 상용화되고 있는 소프트웨어와 비교 했을 때 유의미하게 높은 상관계수를 나타냈다 (유의 확률 < 0.001).

결론

결론적으로, 이 결과는 새로 개발된 위치 적응형 한계치 방법을 사용하는 소프트웨어가 관상동맥 질환을 판단하는데 보조 시스템으로서 잠재력이 있다는 것을 보여준다.

파트 2. 전산화 단층촬영 영상을 이용한 칼슘의 블루밍 아티팩트 분석 연구

서론

전산화 단층촬영은 널리 알려진 비침습적 방법으로 관상동맥 질환 진단에 사용된다. 하지만, 전산화 단층촬영에 나타나는 칼슘의 블루밍 아티팩트는 관상동맥 내강 면적의 과소평가를 유발한다. 기존 연구들은 주관적으로 시각적 평가를 하였을 때, 높은 엑스레이 에너지를 통한 전산화 단층촬영이 칼슘의 블루밍 아티팩트를 줄일 수 있다고 제안하였다. 이 팬텀 연구는 전산화 단층 촬영 영상에서 나타나는 칼슘으로 인해 밝아진 주변 픽셀에 대해 객관적이고 정량적으로 측정하고, 높은 엑스레이 에너지와의 관계를 분석하고자 하였다.

방법

칼슘의 다양한 모양과 크기를 고려한 팬텀을 제작하였다. 세 개의 이중 에너지 전산화 단층촬영기법을 (지멘스 [벤더 1], 필립스 [벤더 2], 그리고 제너럴 일렉트릭 [벤더 3]) 통해 최대 관전압, 킬로전자볼트의

변화에 따른 팬텀 이미지를 획득하였다. 칼슘으로 인해 밝아진 주변 픽셀은 칼슘 최대 밝기 3분의 1이 되는 값들의 폭을 통해 결정된 실제 칼슘 영역을 (평균 에러 = 0.05 mm, 평균의 표준오차 = 0.01 mm) 제외하고 측정하여 분석하였다.

결과

재건된 다색 전산화 단층촬영 영상에서 최대 관전압의 변화는 칼슘으로 인해 밝아진 주변 픽셀을 줄이는데 영향을 미치지 않았다 (벤더 1, 2, 그리고 3에 대하여 시야 300 mm, 유의 확률 = 0.167, 0.494, 그리고 0.861; 시야 150 mm, 유의 확률 = 0.150, 0.161, 그리고 0.075). 이에 더하여, 킬로전자볼트의 변화는 세 개의 이중 에너지 방법을 통해 얻은 가상 단색 재구성 영상에서 칼슘으로 인해 밝아진 주변 픽셀에 대한 다른 양상을 보였다 (벤더 1, 2, 그리고 3에 대하여 시야 300 mm, 유의미한 차이 없음 [유의 확률 = 0.191], 증가 [유의 확률 < 0.001], 감소 [유의 확률 < 0.001]).

결론

객관적이고 정량적인 측정 방법을 통해 관찰하였을 때, 높은 엑스레이 에너지 레벨과 칼슘으로 인해 밝아진 주변 픽셀은 관계가 없다는 것을 나타냈다.

주요어: 관상동맥질환, 전산화 단층촬영, 새로운 위치 적응형 한계치 방법, 블루밍 아티팩트, 엑스레이 에너지, 칼슘으로 인해 밝아진 주변 픽셀

학번: 2021-39269